République Algérienne Démocratique et Populaire
Ministère de l'Enseignement Supérieur et de la Recherche Scientifique

Université Amar Thelidji- Laghouat

FACULTE : DE TECHNOLOGIE

DEPARTEMENT : D'ELECTRONIQUE

MEMOIRE DE MASTER

Présenté par :

Zaazaa Khaoula OPTION : Microélectronique

Boumegouas Khadhra OPTION : Microélectronique

DOMAINE : Sciences et Technologie

FILIERE : Electronique

Thème

Modeling of Plasmonic light-trapping design in ultrathin GaSb thermophotovoltaic cell

Jury de soutenance :

Nom et Prénom	Grade	Qualité
Mouhoub Birane	MCA	Chairman
Vilbois Leila	MAA	Examiner
Fathi Bendelala	MCA	Supervisor
Ali Cheknane	prof	Co-supervisor

Promotion : 2022/2023

بسم الله الرحمن الرحيم

وَقُلِ اعْمَلُوا فَسَيَرَى اللَّهُ عَمَلَكُمْ وَرَسُولُهُ وَالْمُؤْمِنُونَ ۖ وَسَتُرَدُّونَ إِلَىٰ

عَالِمِ الْغَيْبِ وَالشَّهَادَةِ فَيُنَبِّئُكُم بِمَا كُنتُمْ تَعْمَلُونَ (105)

صدق الله العظيم .

ACKNOWLEDGEMENTS

First and foremost, we thank Almighty **God** who help us to complete this study and who inspired us with health, wellness, and determination, so thanks **God**.

We extend our sincere thanks and appreciation to our supervisors Dr. **Fathi BENDELALA** and Prof. **Ali CHEKNANE** for all the pieces of advice and valuable understanding and give us this opportunity to discover this interesting scientific domain. Finally, we wish to extend our sincere thanks to the members of the esteemed discussion committee, and our gratitude to all of our professors at Amar Teliji University of Laghouat.

DEDICATIONS

This manuscript is dedicated to my lovely **Mother** and **Father**. Without their endless love and encouragement, I would never have been able to complete my graduate studies. I love you both and I appreciate everything that you have done for me, and also my brother (**Mohamed**) and my sweet sisters (**Rima, Soraya Noura, Farah, aya,** and **Fatima**), and my friends (**Safa, Khadhra, lamia, Rym, Abir, Rachida** and **Imane**), and all who supported me.

I also dedicate this graduation work to the soul of my dear **Grandmother** may **God** have mercy on you and grant you paradise. Many thanks to my generous **Husband** for supporting me, my **Father**, my **Brothers**, my **Friends**, and all my **Family**.

NOMENCLATURE

TPV	Thermophotovoltaic
MTM	Metamaterial
μ	Magnetic permeability
ε	Electric permittivity
n	Index of refraction
D	Electric flux density or electric displacement ($C.m^{-2}$)
B	Magnetic flux density (T)
E	Electric field ($V.m^{-1}$)
H	Magnetic field ($A.m^{-1}$)
ω	Angular frequency (Hz)
K	Wave number
c	Speed of light ($m\ s^{-1}$)
W	Tungsten
q	Charge of electron ($1.60217657 \times 10^{-19}$ C)
Γ	Damping Constant
ω_p	Plasma frequency
ε_0	Permittivity free space (8.85 x 10-12 F/m)
$Z(\omega)$	Frequency-dependent impedance
SRR	Split ring resonator
TE	Transverse electric
TM	Transverse magnetic
CST	Computer simulation technology
HFSS	High-frequency simulator system
FEM	Finite element method
IR	Infrared
TBB	Blackbody temperature
σ	Electric conductivity ($s\ m^{-1}$)
$\hbar$	Plank's constant ($6.62606957\times10^{-34} m^2 kg s^{-1}$)
K	Boltzmann's constant ($1.3806\times10^{-23}\ m^2 kg\ s^{-2} K^{-1}$)
$e(\omega)$	the emittance of the metamaterial emitter
FF	fill factor
J_{ph}	photocurrent generated ($A\ m^{-2}$)
EQE	External quantum efficiency
η_{TPV}	Thermophotovoltaic cell efficiency
E_g	Bandgap energy
$\vec{k}$	wave vector
$\overrightarrow{E}$	Electric field
$\overrightarrow{H}$	Magnetic field
$\vec{S}$	Poynting vector

χ_e	electric susceptibility
χ_m	magnetic susceptibility
T_{BB}	Blackbody temperature
λ_{gap}	Bandgap wavelength
η_{diode}	diode efficiency
η_{sp}	spectral efficiency
P_{abs}	Absorbed power
P_{rad}	Radiated power
P_{out}	Output power
V_{oc}	open circuit voltage
I_{SC}	short circuit current
I_{MPP}	The current of Maximum PowerPoint
V_{MPP}	The voltage of maximum PowerPoint
$\alpha(\omega)$	Absorption
SPPs	Surface Plasmon Polaritons
IQE	internal quantum efficiency
MP	Magnetic polariton
FP	Fabry Perot

Table of Contents

List of Figures

List of Tables

Abstract

This manuscript studies the potential of using a light-trapping strategy based on a Metamaterial structure, which is made for enhancing photon absorption in ultrathin gallium antimonide (GaSb) Thermophotovoltaic (TPV) cells. Through the use of the rigorous Finite Element Method (FEM), and Finite Difference Time Domain (FDTD) approaches using the powerful software CST, it was found that this nanostructured configuration can excite: magnetic polariton (MP), surface plasmon polariton (SPP), and Fabry-Perot (FP) resonances, leading to increased absorption in the active layer. Further discussion was conducted on the influence of geometric parameters, polarization sensitivity, and incidence angle in the absorption peak yielded. Finally, the electrical proprieties with the conversion efficiency of the ultrathin TPV cell-coupled Metamaterial structure have been computed. The maximum cell efficiency that can be obtained is 11.3% under blackbody radiation of 2000k, which is induced by the MP, SPP, and FP phenomena, and directly contribute to enhancing cell conversion efficiency.

Keywords: *GaSb TPV cells, thermophotovoltaic; ultrathin TPV cell, Plasmonics, Metamaterials, light trapping.*

ملخص

تدرس هذه المخطوطة إمكانات استخدام إستراتيجية حبس الضوء على أساس هيكل المادة الخارقة، والذي تم تصميمه لتعزيز امتصاص الفوتون في الخلايا الحرارية (GaSb) التي تحتوي على مادة حرارية ضوئية (TPV). من خلال استخدام طريقة العناصر المحدودة الصارمة (FEM) ونهج المجال الزمني للفرق المحدود (FDTD) باستخدام البرنامج القوي CST ، تم التوصل أن هذا التكوين النانوي يمكن أن يثير: البولاريتون المغناطيسي (MP) ، البولاريتون السطحي للبلازمون (SPP) ، وصدى فابري بيروت (FP) ، مما يؤدي إلى زيادة الامتصاص في الطبقة النشطة. تم إجراء مزيد من المناقشة حول تأثير المعلمات الهندسية ، وحساسية الاستقطاب ، وزاوية السقوط في ذروة الامتصاص الناتجة. أخيرًا ، تم حساب الخصائص الكهربائية مع كفاءة التحويل لهيكل الموارد الغير الطبيعيه المرتبط بالخلايا شديد الرقة. الحد الأقصى من كفاءة الخلية التي يمكن الحصول عليها هو 11.3٪ تحت اشعاع مصدر حراري K2000، وهو مرتبط بظواهر MP و SPP و FP ، ويساهم بشكل مباشر في تعزيز كفاءة تحويل الخلية.

كلمات المفتاح: خلايا GaSb ، الكهروضوئية ؛ خلية TPV فائقة الرقة ، بلازمونيكس، المواد الخارقة ، محاصرة الضوء.

General introduction

Ultrathin cells have gained increasing attention due to their potential for reduced weight, reduced cost and increased flexibility. However, the light absorption in ultrathin cells is usually very weak compared to the corresponding bulk cells. To achieve enhanced photon absorption in ultrathin thermophotovoltaic (TPV) cells, this work proposed a film-coupled metamaterial structure made of nanometer-thick gallium antimonide (GaSb) layer sandwiched by a top one-dimensional (1D) metallic grating and a bottom metal film.

Outline of the manuscript

Chapter 1: First, starting with a short historical brief of the Thermophotovoltaic (TPV) conversion system. Then, the functionality of TPV systems, and their different components: Heat sources, the spectral control concepts (selective emitters, filters). Further, low-gap TPV cells are presented near close by their classification. **Chapter 2**: This chapter presents an important aspect of Metamaterials (MTMs) research. The definition of metamaterials along with a historical overview is briefly discussed. The recent interest in metamaterials and progress in the development of this research area is briefly discussed, Moreover, we elucidate three major categories of electromagnetic MTM, namely electric MTM ($\varepsilon < 0$), magnetic MTM ($\mu < 0$), and negative index of refraction ($n < 0$) MTM. **Chapter 3:** This chapter presents an introduction to Plasmonic and Surface Plasmon Polaritons phenomena, as well as plasmonic light trapping configuration and optimization guidelines, a short investigation of surface plasmons polariton (SPP) in metallic nanostructures based on metals has been represented, and which would be employed to create more confined modes for Thermophotovoltaic and Photovoltaic applications. **Chapter 4: T**his chapter

has been consecrated for the numerical simulation of ultrathin TPV cell based on Metamaterials configuration, the optical proprieties have been extracted using finite-element method (FEM) and FDTD Methods, a detailed discussion of their various characteristics such as absorption rate, polarization sensibility for different incidence angle, then the electrical parameters with overall conversion efficiency of the TPV system has been computed for a temperatures range from 1000 up to 2000K. Noteworthy, involving the light-trapping strategy, the absorption rate can be improved and tailored for a true external quantum efficiency (EQE) of TPV cell

. La mise à jour automatique des citations est désactivée. Pour voir la bibliographie, cliquez sur Actualiser dans l'onglet Zotero. ADDIN ZOTERO_ITEM CSL_CITATION {"citationID":"a174c2arm6n","properties":{"formattedCitation":"\\uldash{[1]}","plainCitation":"[1]","noteIndex":0},"citationItems":[{"id":245,"uris":["http://zotero.org/users/11189872/items/S6IT5FMW"],"itemData":{"id":245,"type":"thesis","title":"Modeling and performances optimization of thermophotovoltaic cells based on new metamaterials","author":[{"family":"Bendelala","given":"F"}]}}],"schema":"https://github.com/citation-style-language/schema/raw/master/csl-citation.json"} [1]

Chapter I: Thermophotovoltaic Conversion System

I .1. Introduction

Our aim in this chapter is to look into the fundamental model of the thermophotovoltaic (TPV) conversion system and clarify their constitutive components, such as the potentially used heat sources, the spectral control mechanism (selective emitter, filter…), with some advantages compared to conventional solar PV. In the far field of their development during the last years, we will be exposed to, and display the current challenges facing TPV conversion systems, with the recent outlook which can in advance improve the efficiency of TPV conversion by meeting the requirements of earlier enhancement techniques, which may give feature ideas of major keys for the TPV efficiency improvement.

I.2. The importance of Thermophotovoltaic conversion

The majority of energy used in today's industrial society is used in the transportation, building, and industrial sectors. Additionally, combustions are the primary sources of this energy. As a result, the use of combustions has given rise to widespread worries about supply security, rising energy demand, and resource limitations for both (local and global) environmental impacts (such as the dangerous acid rain and climate change) [1]. As a result, there is growing interest in alternative energy sources and in using combustions effectively. Additionally, according to Carnot's theory of energy conversion, the TPV system may be able to convert heat into electricity, making it an attractive alternative to the current generation of electricity technologies[1].

The TPV conversion method has some inherent technological advantages over the current methods for electricity supply [1]. Large amounts of waste heat produced during the conversion are a drawback of central power generation. Even for contemporary combustion-powered and combined-cycle power plants, waste heat inputs are about half of the outputs. The system's

complexity, problems with security supplies like blackouts, and distribution and transmission losses are just a few of the drawbacks. However, to reduce inefficiency and lower maintenance costs and noise levels, central power supply technologies must be scaled back. Large-scale fossil power plants can be replaced by renewable generators (wind, solar PV). Additionally, their widespread use requires high scale and high economic power [2].

On the other hand, a large portion of non-grid-connected electricity comes from rechargeable batteries, which have some drawbacks in terms of a limited lifetime, as well as a slow charging process, and low gravimetric energy density (*MJ/kg*). These drawbacks are offset by the small scale range of power, most likely at the order of hundreds of watts to a few milliwatts, and the fact that a large portion of non-grid connected electricity comes from rechargeable batteries. Hydrocarbon fuels are easy to store and can be supplied quickly, and their gravimetric energy densities are typically 100 times higher [2].

I.3. Comparison of TPV with PV conversions

A TPV system operates on the same principle as a photovoltaic (PV) system, but the primary energy source is the emitter's near-infrared radiation, which can be heated by an external energy source like the combustion of gas, liquid, or nuclear fuel, as shown in figure 1.1, or even the waste heat from a glass-making furnace [3]

The actual primary variations between TPV and PV systems are [4],[5]:

- The temperature level is much higher than, for instance, PV solar cells, whose input power is only 1 $kW.m^{-2}$ when high-power output devices with output powers of 10–20 $kW.m^{-2}$ have already been fabricated.

- In PV systems, the sun produces almost blackbody radiation at temperatures of like 6000 K for a distance of 150 x 106 *km*. In contrast, in thin-film photovoltaic systems (TPV), the radiators/emitters emit at temperatures of (1500 to 1800 K) for distances of the order of a few centimeters, as we illustrate in Figure 1.1, [6], [3].
- Supply and demand are in phase, which gets around one of the biggest issues with solar energy production—that it only occurs when the sun is shining. Hybrid solar thermal systems are an option, and some of them have already been put into use. Such a system uses oil or molten salts to store the extra heat generated by solar panels. TPVs can then be utilized to produce electricity at night [7].
- TPV systems can be powered by a variety of fuels, including solar energy, used industrial heat, gas burners, and theoretically even nuclear generators.
- TPV devices are ideal for use in remote locations or as portable power sources, such as for military applications, because they are lightweight and have no moving parts, making them quiet and low-maintenance.

The quality of the TPV converter cells themselves and insufficient efficiency for cooling the devices are the main issues that TPV systems currently display. While additional study is required to enhance the quality of the cells and spectral control elements of TPV conversion, a cooling system could be used to generate heat simultaneously.

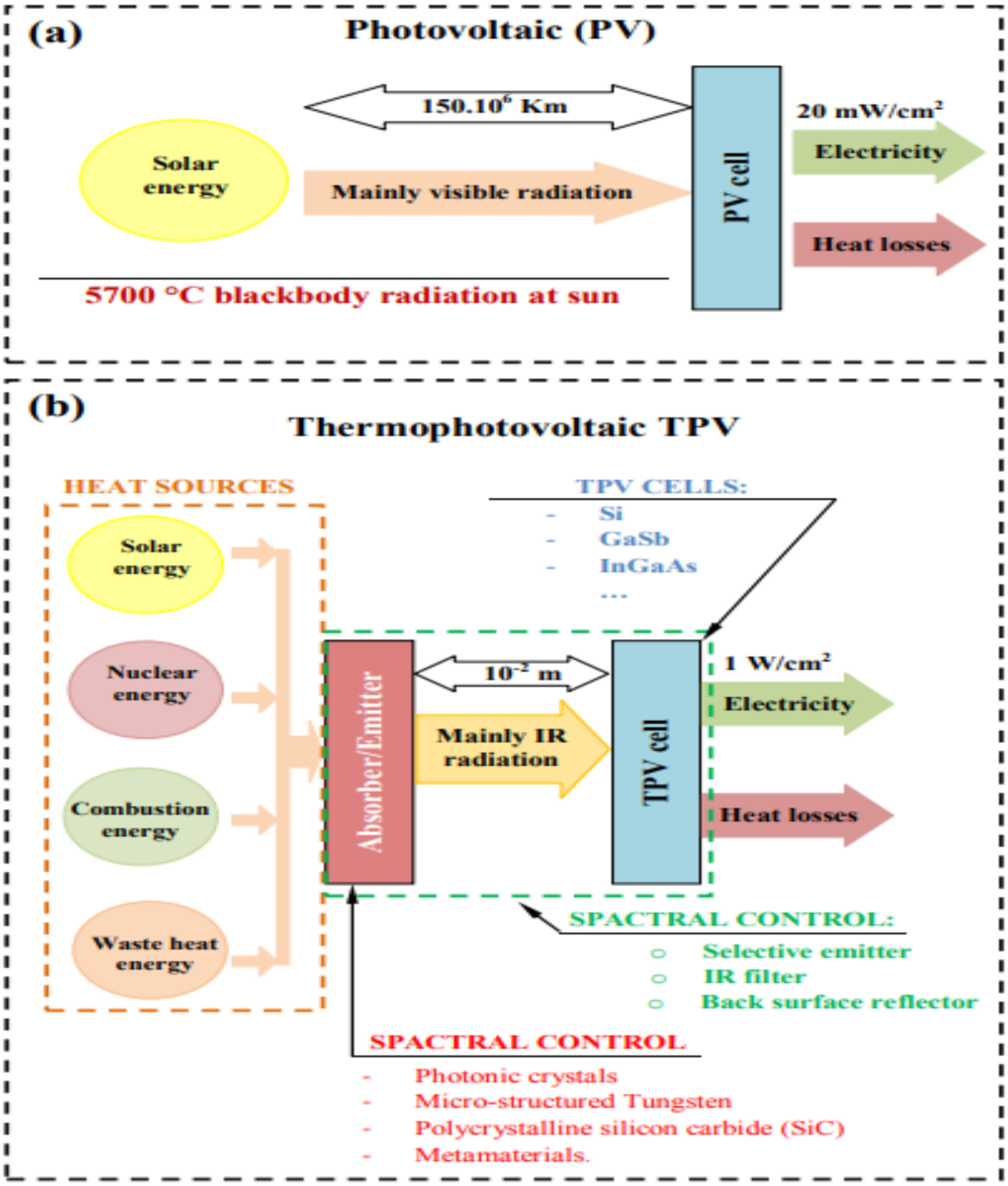

Fig.1. 1: Photovoltaics versus thermophotovoltaics *[5]*

I.4. Operating principle of the TPV system

I.4.1. Components of the TPV system

Electricity production using TPVs is a highly interdisciplinary technology. Several thermo-physical phenomena relating to the various components of the TPV system are involved in the conversion of thermal radiation from the heat source into electricity.

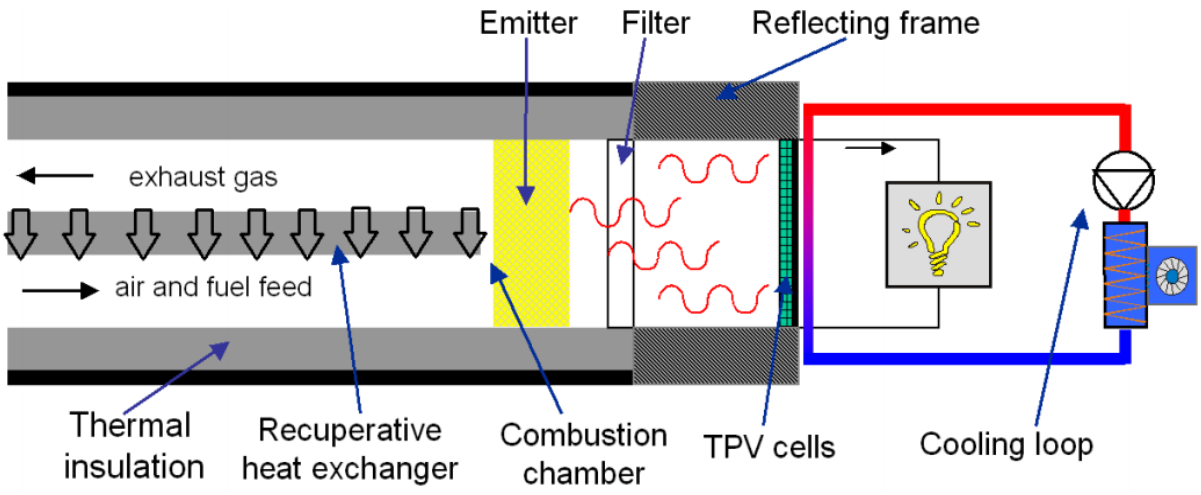

Fig.1. 2: Simple scheme of a fueled TPV system *[5]*

The following are the primary parts of a TPV device [4]:

- **Heating system:** Heating system: It emits the heat energy necessary to warm the emitter component. A TPV device can use any heating method (such as a recuperative burner, solar concentrator, or nuclear reaction) to provide thermal power;
- **Optical system:** To reduce radiation losses between emitter and cells, it is made up of an emitter, a filter, and a reflecting frame. The primary purpose of the optical system is to

transform the heating system's heat energy into radiation and transfer it to the cells while simultaneously realizing a spectral selection of radiation.

- **TPV cells:** They transform radiation into electricity. The radiation density is very high, so their design differs slightly from that of a typical PV cell. For the same reason, using a cooling system to lower their temperature is essential to prevent damage.

Figure 1.2 depicts an example design for a fueled-TPV system. In this instance, a combustion chamber and a recuperative heat exchanger make up the heating system. Since a TPV device is made up of various parts, its overall efficiency can be thought of as the sum of all the efficiencies related to each energy transfer that occurs in the system.

I.4.1.1 Heat sources available for TPV conversions

The ability to heat up the absorber/emitter component using any blackbody heat source is a remarkable benefit of TPV technology. TPV is a flexible technology because it only needs enough temperature energy to complete the conversion. Based on various conventional and unconventional heat sources, numerous studies for TPV structures have been proposed. It is recapped in Ref [4] as follows:

- **Nuclear-fuelled TPV** was designed for deep space missions and is based on a radioisotope general-purpose heat source (GPHS) [8].
- **Bio-fuelled TPV** is based on wood-powder combustion [9].
- **Concentrated Solar TPV**, wherein an optical system (mirrors or lenses) can focus solar radiation on a TPV cell to a concentration ratio of up to 4600X [10].
- **Heat sources are realized by the combustion of either gaseous fuel** (like propane, natural gas, or methane) or liquid fuel (like diesel or hydrocarbon fuels) [11].

Because of their temperature, bodies emit thermal radiation. A blackbody is regarded as a perfect radiation absorber by definition. Since all materials will reflect some radiation, it is a perfect idea. A blackbody is regarded as the ideal source of thermal radiation [12].

Planck's law of radiation [5], [4], states that a blackbody (thermal heat source) emits its full power per unit bandwidth per unit area ($Wm^{-2}\ m^{-1}$):

$$E(T_{BB},\lambda)=\frac{2\pi.h.c^2}{\lambda^5}.\frac{1}{(e^{\frac{hc}{\lambda KT_{BB}}}-1)} \qquad \textbf{Eq(1. 1)}$$

Where represents the Planck constant (6.626×10^{-34} Js), the blackbody temperature (°C), the light speed (2.98×108 *m/s*), the Boltzmann constant (1.380×10−23 *JK*), and the wavelength (*m*). The total thermal radiation emitted over the entire wavelength spectrum corresponds to the total power density emitted by a thermal source.

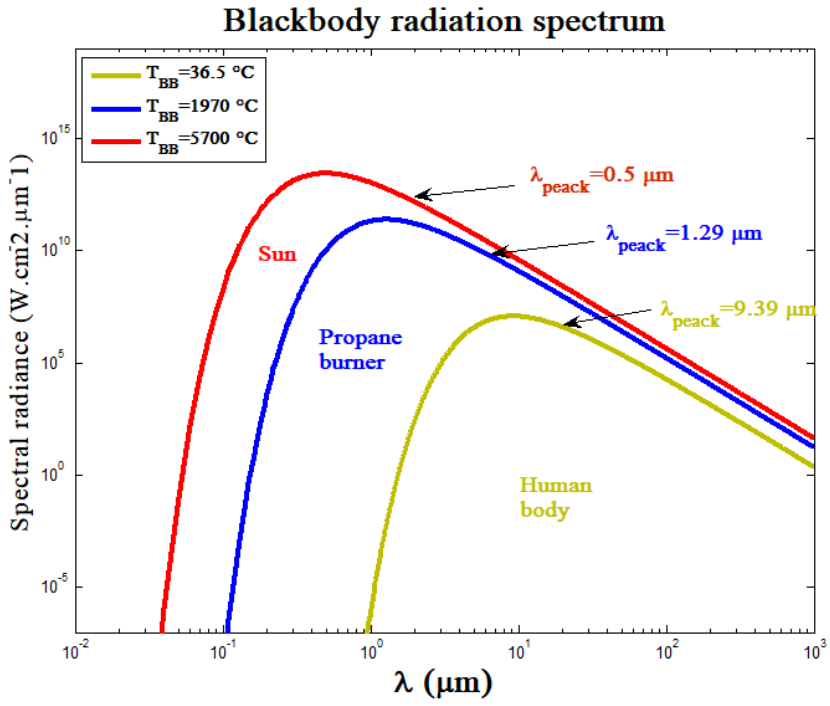

Fig.1. 3: Spectral radiance for selected blackbody temperatures (T_{BB}).

Additionally, we display in Figure 1.3 objects with chosen maximum temperatures for solar cells (red line), TPV devices (blue line), and IR photon detectors, as well as the spectral emittance of a blackbody that is determined by Equation (1.1). (green line). The lowest emission wavelengths are at about 36.5 °C, while the highest emission wavelengths are at about 5700 °C.

I.4.1.2 Spectral control components

For the TPV cells to convert energy successfully, spectral control is necessary. A small portion of the total radiant energy is necessary for the conversion of TPV; typically, it is less than that. For instance, at 950 °C T_{BB} (blackbody temperature), and 0.52 eV is the TPV cell band gap, only about 27% of the total radiant energy can be converted to electricity. The remaining 73% of radiant energy cannot be converted into electricity [13], so to increase TPV efficiency, this unconvertible energy must either be suppressed from being emitted from the source or completely reflected back. And we can conclude that TPV conversion energy performance and efficiency have significantly declined in the absence of a spectral control.

$$\eta_{TPV} = \eta_{cell} \times \eta_{Spectral} \qquad \textbf{Eq(1. 2)}$$

η_{TPV}: the efficiency of a thermophotovoltaic system

η_{cell}: the efficiency of TPV Cell

$\eta_{Spectral}$: the efficiency of spectral control

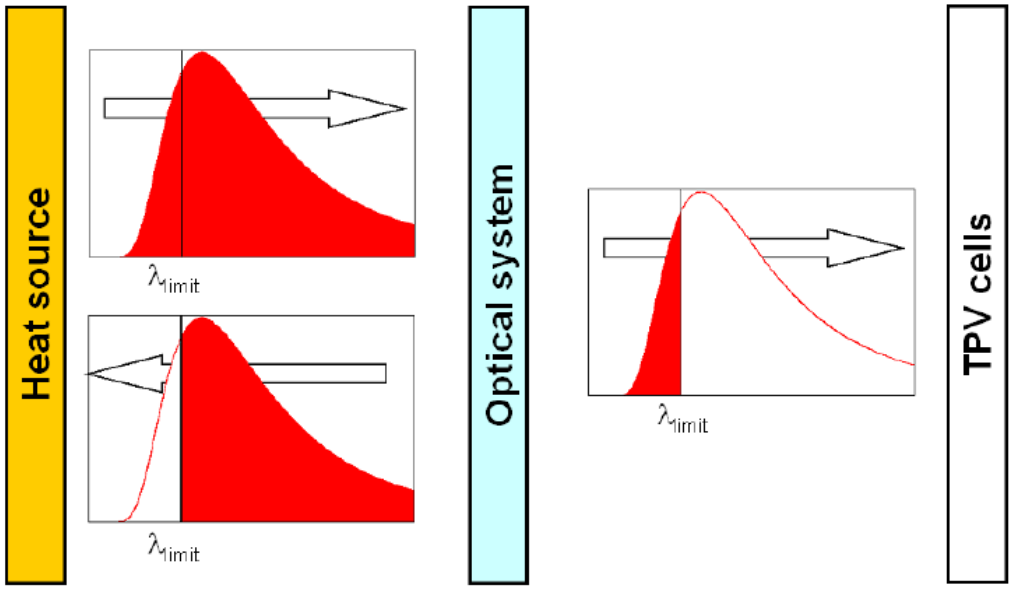

Fig.1. 4: Operating principle of TPV spectral control [14].

Figure 1.4 illustrates an elementary design for the optical system concept and explains how the optical system works to increase efficiency. An explanation of spectral control mechanism is a system that only emits wavelengths that correspond to the gap and reflects all wavelengths that have the gap. Thus, conversion efficiency would increase.

1. Absorber/Emitter component

This part, also known as a "radiator," can be either a selective or a broadband absorber/emitter. It can be categorized based on a variety of factors, including the following [1]:

- Optical properties (e.g. absorption, emissivity, polarization sensitivity).
- Thermal properties (e.g. melting point, upper operation temperature, evaporation rate).

- Electrical properties
- Material composition.
- Design shape (e.g.1D, 2D, and 3D Photonic crystals (PhCs) structure. micro-structured).
- Availability and economics

Oil, gas, or even wood burners can be used to heat the absorber/emitter in a traditional TPV system. The most recent absorber/emitter technology for TPV application can be essentially summarized in four different innovative prototypes, which are commercially available for large-scale power ranging from a few *kW* to a few *MW* for immobile applications [15].

- One of the most popular materials for broadband ceramic absorbers/emitters is silicon carbide (SiC), which has a good emittance of 0.9% across the entire infrared spectrum [16].
- The use of 1D, 2D, and 3D Photonic Crystals (PhCs) structures is a cutting-edge method to design selective absorbers/emitters. Depending on the periodicity of the unit cell structure, PhCs intervene by employing their optical band-gap to suppress the (emissivity=emittance) in a particular spectral range. The increase in selectivity of tungsten surfaces involving PhCs band-gap properties is demonstrated experimentally by Celanovicet al. [17].
- Micro-structured tungsten is an additional method for creating a selective emission for TPV applications; this absorber/emitter is advised for use in a TPV system with GaSb. Unfortunately, the design uses a convoluted conception process and its emittance strongly depends on the angle [18].

- Recently, many theoretical and experimental studies on high-temperature selective emitters have been conducted to help reach 24% of efficiency. There are several approaches, such as selective Metamaterial emitter (SME), selective Meta-surfaces (FSSs), etc… [19].

2. Optical Filter

In order, to reflect all wavelengths that are out of the photovoltaic cell's band gap, optical filters, and reflectors are typically positioned between the emitter and the photovoltaic cell. Four different categories can be used to categorize TPV filters [5] s:

1. Quartz glass: With high emittance values at some wavelengths and high transmittance values at others, it functions as an absorptive filter. In a TPV system, quartz glass is typically used to shield the TPV cells from extreme heat and to achieve a first selection of radiation that lowers the thermal charge on the cells [4].
2. Interference (or dielectric) filters are low-pass filters that are realized as a multilayer stack of thin dielectric films. In essence, they are made of two materials one with a high and one with a low refractive index [1].
3. Plasma filters based on Transparent Conducting Oxides (TCOs): Referred to as Plasma filters, these devices are made of a highly doped semiconductor layer and have optical characteristics similar to those of insulators with low absorption and a wide reflectance range [8].
4. Frequency Selective Surface (FSS) filters, also referred to as Meta-surfaces filters (MSFs) are constructed from a collection of refractory metallic nano-patch elements that have been deposited on a dielectric substrate. They are fantastic candidates for TPV applications because of their spectral selection properties [20].

I.5. TPV cells technologies

The primary application of TPV cells relies on the photogeneration of electrons and charge carrier separation. The energy of the photon is absorbed by an electron with the highest energy level and bound to nearby atoms (electron in the valence band), exciting it to an energy level where the electron is free to move and generate current. This process produces an electron-hole pair when a photon with energy greater than the semiconductor band gap strikes a semiconductor material (conduction band). Another electron in the valence band may occupy the hole left by the absence of an electron [4]. Diffusion length refers to the average path taken by charge carriers before recombination. a semiconductor's bandgap (also known as the cell bandgap Eg)

The p-n junction sector of the cell, which is made up of a layer of the n-type (high number of electrons) and a layer of the p-type (high number of holes) put together in close contact, separates the photo-generated charge carriers. Large-area p-n junctions are found in TPV cells [1]. The diffusion of electrons into the p-type layer and their subsequent recombination with the holes there are caused by the electron in the n-type layer. An electric field produced by the unbalanced charge distribution balances this diffusion current.

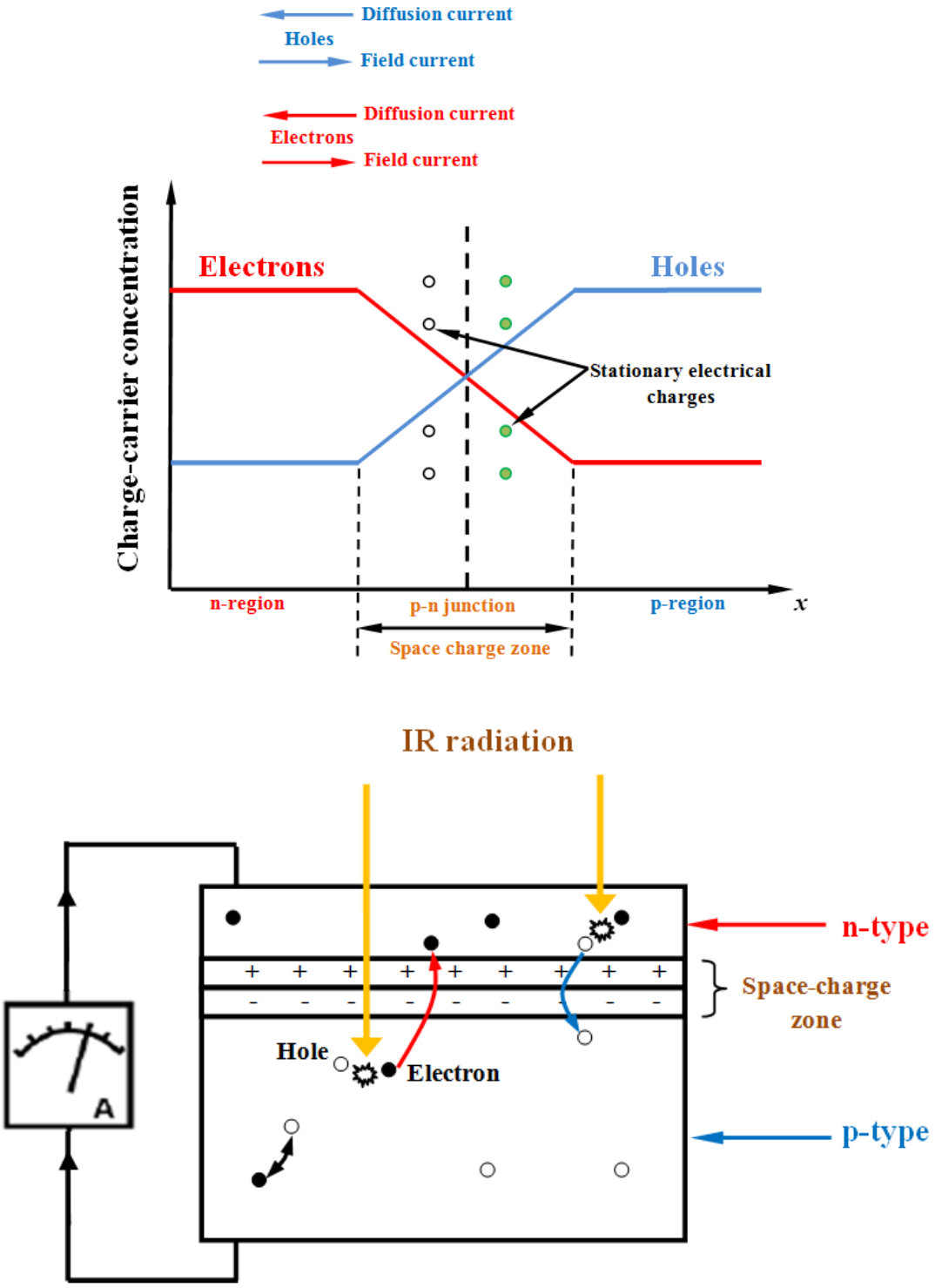

Fig.1. 5: Distribution of charge carriers at a p-n junction and operating principle of a TPV cell [14].

Under the same circumstances, there are no moving charge carriers in the region near the junction known as the "space-charge zone." If an electron-hole pair is created after the absorption of a photon with sufficient energy, the electric field created by diffusion serves as a separation zone: if the pair is created on the p-side, the electric field accelerates the electron into the n-side, and vice versa [1]. The generated hole is brought into the p-side if the absorption occurs on the n-side, as shown in Figure 1.5.

When there is no connected load in the TPV cell, the photo-generated current is at its maximum. When the load is connected to the TPV cell, the photo-generated current from cell illumination results in negative voltage, and the Shockley diode equation [4] describes the current-voltage characteristic I(V) curve of a diode:

$$I_{diode} = I_0\left[\exp\left(\frac{qV}{KT}\right)-1\right] \qquad \textbf{Eq(1. 3)}$$

q: electron charge (1.6×10^{-19} C).
V: the voltage across the diode.
K: Boltzmann constant.
T: represents the absolute temperature.
$\boldsymbol{I_0}$: represents diode current saturation.

I.5.1. Electric properties of TPV cells

Open circuit voltage (V_{oc}), short circuit current (I_{sc}), and maximum power point are the three primary properties of TPV cells (V_{mp}, I_{mp}). The bend in the I-V curve known as the maximum energy point is where the TPV cell's maximum power is produced [5].

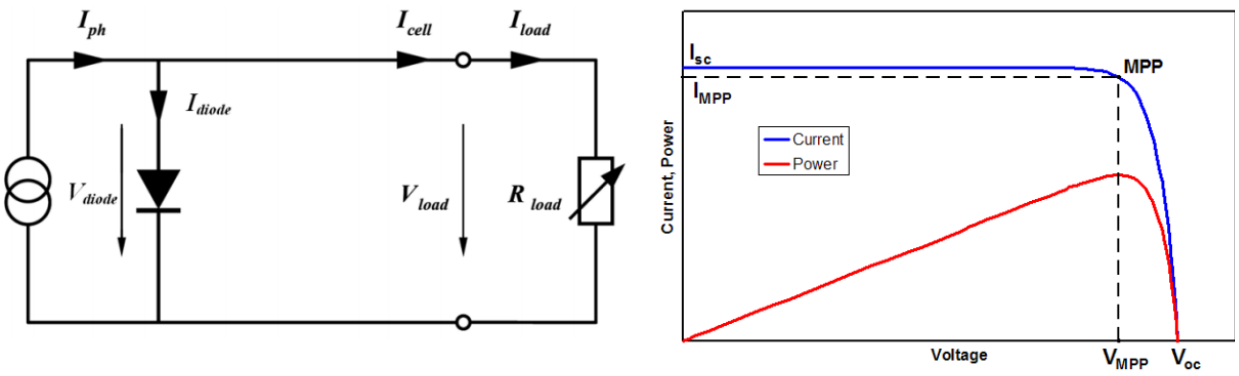

Fig.1. 6: Equivalent circuit of an ideal TPV cell, and qualitative (IV) and power curve of a TPV cell [20].

Therefore, the equivalent circuit for a perfect TPV cell consists of a parallel connection of a photocurrent source (I_{ph}), a diode, and a resistor (R_{load}), as shown in Figure 1.6. In the best scenario, the current passing through the load yields [21]:

$$I_{cell} = I_{ph} - I_{diode} = I_{ph} - I_0\left[\exp\left(\frac{qV}{KT}\right) - 1\right] \qquad \textbf{(Eq1. 4)}$$

The power increases as the load increases, peaking at the so-called Maximum Power Point (MPP) following the Maximum Current Point (I_{MPP}) and Maximum Voltage Point (V_{MPP}), also known as open circuit voltage (V_{oc}). For higher values of E_g and constant blackbody radiation, Isc decreases and we receive fewer photons with energy above E_g, whereas V_{oc} increases. The Fill-Factor is yet another crucial element of photovoltaic characteristics (FF). The fill factor determines the quality of the TPV cell. It operates way better when the FF value is close by to unity [10].

$$FF = \frac{V_{MMP} \times I_{MMP}}{V_{OC} \times I_{SC}} \qquad \textbf{Eq(1. 5)}$$

Figure 1.7 depicts the equivalent circuit of a real TPV cell, with a parallel resistance (R_{sh}) representing leakage currents due to impurities caused by a partial shorting of the p-n junction, and a series resistance (R_s) representing leakage currents due to material resistance and the resistance of the cell surface metallic contacts [21].

$$I_{cell} = I_{ph} - I_0\left[\exp\left(\frac{q}{KT}\left(V_{load} + R_s.I_{cell}\right)\right) - 1\right] - \frac{\left(V_{load} + R_s.I_{cell}\right)}{R_p} \qquad \textbf{Eq(1. 6)}$$

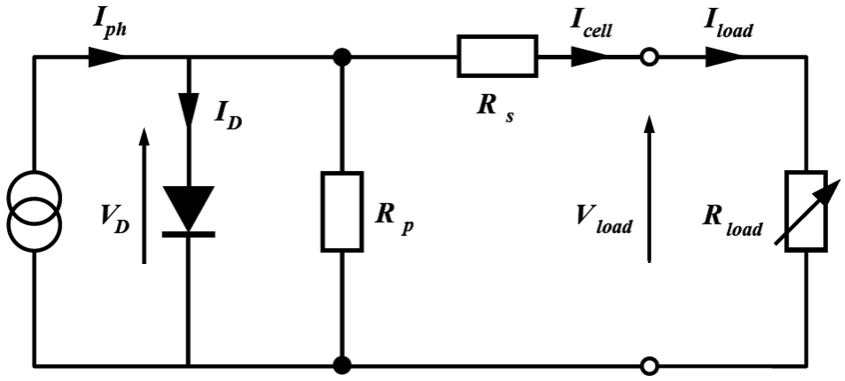

Fig.1. 7: Equivalent circuit of a real TPV cell [21].

The cell temperature is another significant factor that affects the performance of the cell. Cell temperature coefficients, which are experimentally measured and calibrated as the percentage variation of the cell parameters compared to temperature level, are typically used to account for the cell temperature [22]. This is how the open-circuit voltage is determined:

$$V_{oc} = \frac{nKT_{cell}}{q} \times \ln\left(\frac{I_{SC}}{I_0} + 1\right) \qquad \textbf{Eq(1. 7)}$$

Where T_{cell} is the temperature of the cell, n is the ideal factor, and I_0 is the reverse saturation current. It is determined how to calculate the V_{mp} of the fill factor in equation (1.5):

$$V_{MP} = V_{OC} - \frac{KT}{q} \ln \left[\frac{\frac{V_{MP}}{KT}}{\frac{q}{}} + 1 \right]$$ **Eq(1. 8)**

Final calculations for the TPV conversion efficiency are as follows:

$$\eta = \frac{I_{SC} \times V_{oc} \times FF}{P_{inc} - P_{ret}}$$ **Eq(1. 9)**

P_{ret} is the power that the TPV cell reflects, where P_{inc} expresses the power of radiation from the cell. The system's energy effectiveness is calculated as follows [23]:

$$\eta_e = \frac{P_{cell}}{P_{Inc}}$$ **Eq(1. 10)**

η_e : refers to the TPV system's power output and system efficiency. The cell's short circuit current density J_{sc} (mA/cm^2) under a clearly defined blackbody spectrum is calculated. It can be stated as[23]:

$$J_{sc} = \frac{1}{hc} \int_0^{\infty} e(\omega) EQE(\omega) d\omega$$ **Eq(1. 11)**

Where the measured external quantum efficiency, $e(\omega)$ is the emittance of the emitter, h is Planck's constant, and c is the speed of light (EQE). That explains how effectively the radiation that is coming in is converted into electricity. In more detail, it is the proportion between the carriers gathered from the solar cell and the number of photons of a specific energy that are incident. Figure 1.8 depicts a quantum efficiency plot as an example.

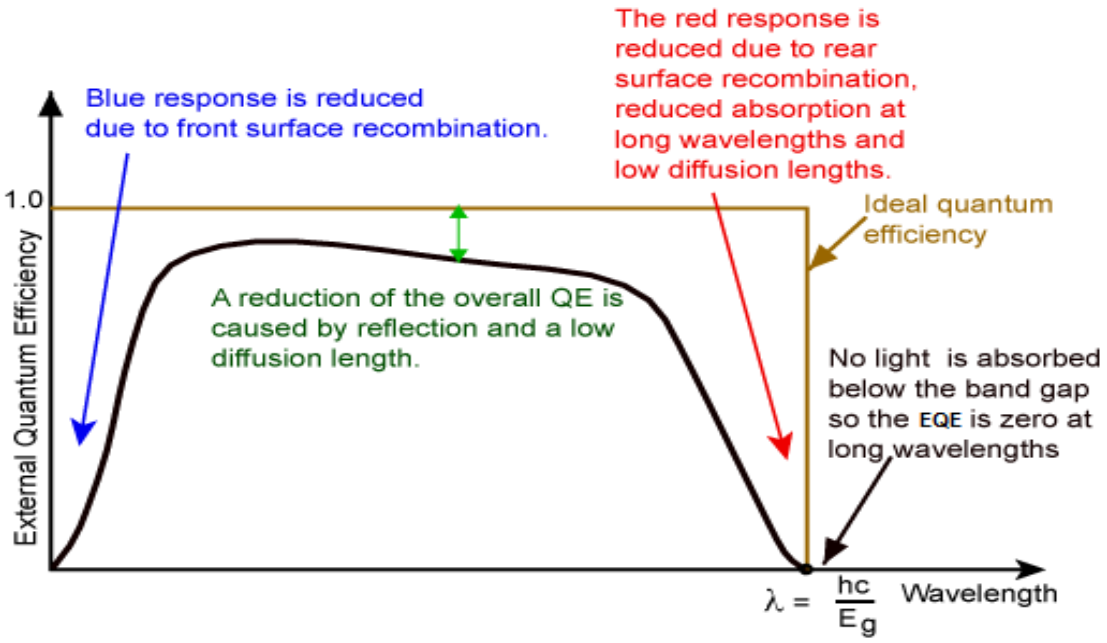

Fig.1. 8: An example of external quantum efficiency plot solar TPV cell vs. ideal quantum efficiency as a function of the wavelength of incoming photons [23].

In a perfect situation, the EQE is equal to 1 if all photons at a particular wavelength are absorbed and the resulting carriers are extracted. The EQE is zero for longer wavelengths because there is no light absorption below the bandgap. Recombination effects cause EQE in real cells to decrease. The processes that reduce the EQE at particular wavelengths are specifically described in the annotations in Figure 1.8. For useful devices, external quantum efficiency (EQE) is frequently measured. It includes optical losses like front-surface reflection. Once all loss mechanisms have been taken into account, it enables a realistic estimation of the performance of manufactured cells. The internal quantum efficiency (IQE) of the devices can be determined by measuring their reflectance and transmission [23].

I.5.2. TPV cell classification

Additionally, TPV cells can be divided into high, middle, and low-bandgap cells:

- High-band gap TPV cells: Due to their high band gap, these cells have low efficiency and need to reach acceptable power density outputs at very high blackbody temperatures (over 1500°C) [19].
- Middle-band gap TPV cells: These TPV cells match the wavelength of the spectrum peak for a blackbody at 1300 °C. For middle TPV systems, cells with Eg=0.7 eV are the most extensively studied; various hetero-structures are created with Eg values ranging from 0.53 to 0.73 eV [24].
- Low-band gap cells: These cells, which have recently been researched and developed and appear appealing for low-temperature applications (less than 900°C), suffer from low V_{oc} voltage and a poor fill factor FF [25].

Year	Material	E_g(eV)	J_{sc} (A/cm^2)	V_{oc} (V)	FF(%)	T_{BB}(°C)	References
1997	InGaSb	**0.7**	0.8	0.38	66	1100	[26]
2000	InGaAsSb	**0.53**	3	0.344	-	1400	[27]
2003	GaSb	**0.72**	3	~0.41	-	Below 1400	[28]
2003	InAsSbP	**0.45**	3	0.15	-	1000	[29]
2003	InGaSb	**0.56**	3	0.26	-	1200	[30]
2004	Two-junction (InGaAs) Junction 1 Junction 2 Total	 **0.74** **0.63** 	 0.303 0.461 0.296	 0.448 0.284 0.724	 61 52 73	 954 	[31]
2004	Ge	**0.66**	10	0.43	-	1500 to 1900	[32]
2006	$InGa_{0.53}As_{0.47}$	**0.74**	1	0.465	64	1000 to 1800	[33]
2006	InGaAsSb	**0.53**	2.9	0.306	67	1800	[34]
2009	$InGa_{0.69}As_{0.31}$	**0.6**	2.26	0.355	66.5	1800	[35]
2011	$Ga_{0.03}In_{0.97}As_{0.81}Sb_{0.13}$	**0.34**	0.29	0.028	33	1000 to 1500	[36]
2013	InGaAs	**0.74**	0.288	0.405	65	Below 2900	[37]
2016	InAs	**0.32**	1.32	0.38	37	Below 1000	[38]
2016	GaSb and GaInAsSb	**0.5 ~ 0.53**	6	0.55	80	800 - 1800	[37]
2017	GaSb/GaInAsSb	**0.53**	7.87	0.8	82	1000 - 1800	[39]
2019	GaAs/GaInAsSb	**0.53**	1.04	0.214	53	800	[40]
2021	In0.2Ga0.8Sb	**0.56**	0.037	0.24	-	N/A	[41]
2021	In0.2Ga0.8As0.17Sb0.83	**0.53**	3.01	0.327	65	300	[41]

Table1. 1: Development of TPV cell technologies [14].

I.6. Advantages and limits of TPV conversion system

A. It makes sense to briefly review the main TPV characteristics after describing and presenting the various processes and components that are typically included in a TPV system to highlight why TPV can be a fascinating and appealing energy conversion technology. The prospective benefit of Strong and dependable technology:

   - ✓ The TPV system requires little maintenance because there are no moving parts.
   - ✓ An important power density output: Power densities higher than 1 Wcm^{-2} can be obtained, which is a hundred times or even higher than typical PV.
   - ✓ The absorber/emitter can supposedly be heated using any heat source.
   - ✓ Due to the spectral control system (such as the absorber/emitter and filter), the cell efficiency is high. These technology's ages are listed below [4]:

B. The primary phenomena that restrict TPV efficiency are also shown in figure 1.9. Only that portion of the incident photon energy that is required to overcome the TPV cell's E_g is useful for creating an electron-hole pair. The excess photon energy enters the semiconductor as heat.

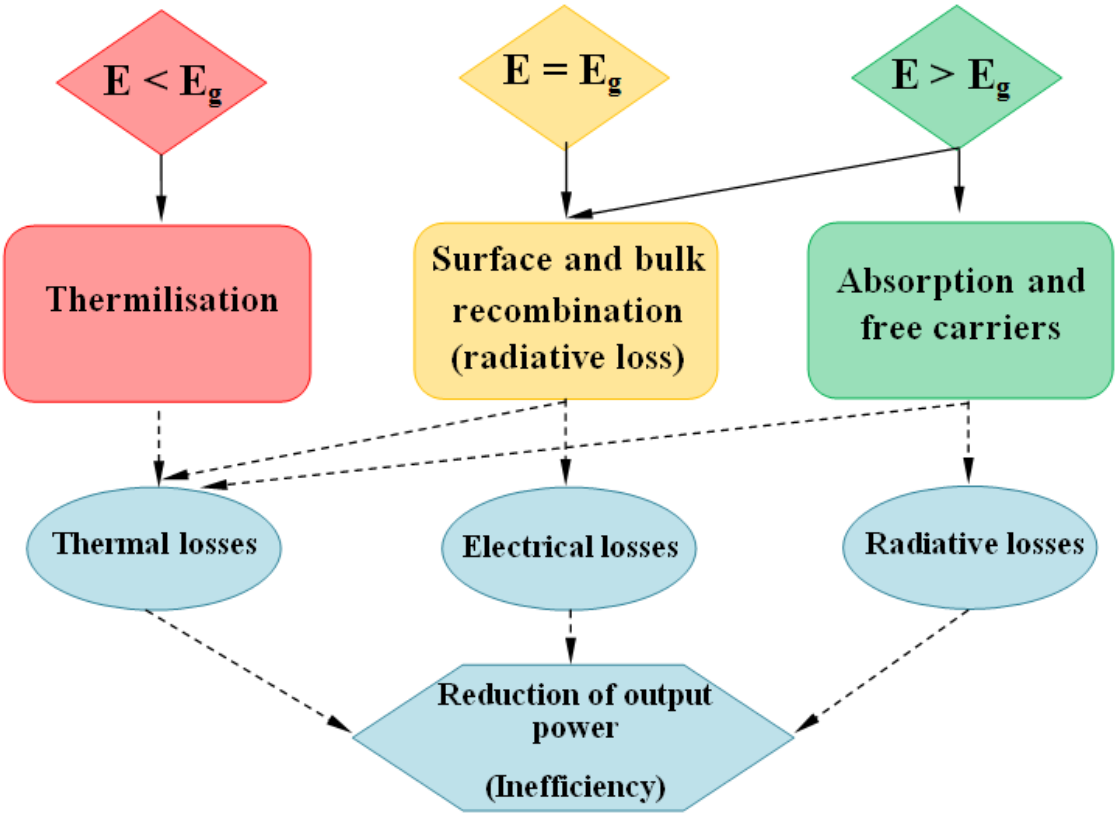

Fig.1. 9: The principal phenomena losses in the TPV conversion system [42]

When it comes to TPV cells, optical losses, and electrical losses are the two main categories of loss mechanisms. The front surface of the cell's reflection, shadowing by the top contacts, sub-bandgap losses, and lattice thermalization caused by extremely high and extremely low-energy photons are some of the main sources of optical losses. Texturing the cell's surface to accept photons from a wide range of incident angles and randomizing the angle at which they enter the cell can reduce reflection losses. Surface texturing, such as Metasurfaces, can be used in conjunction with a back surface reflector to significantly lengthen the optical path of photons inside the semiconductor, thereby increasing the likelihood that they will be absorbed. Light trapping is the name of this technique. Sub-bandgap (thermalization) losses resulting from the fact that not all of the incident spectrum can be used because photons with low energy won't be

absorbed in the cell, which lowers the output current. Single-junction cells make it difficult to get around this problem, but multi-junction cells, which connect several cells with various bandgaps in parallel, can be used to increase the absorption spectrum or an intermediate emitter can be added (selective emitter). Lattice thermalization, the final optical loss, is brought on by energetic electrons. An electron is excited to the conduction band using energy equal to the material's bandgap, and any extra energy is converted to heat. This raises the cell's temperature, which leads to the formation of more defects, narrows the bandgap, and lowers the output voltage.

In low bandgap materials with higher carrier densities, where the interactions between carriers are stronger, Auger recombination is the most significant electrical loss for TPV. In the Auger recombination process, two similar carriers collide; one is excited to a higher kinetic energy, and the other recombine across the bandgap, transferring its energy to a different carrier. Eventually, the extra energy is released as heat, which helps the lattice to become thermalized. Since it is inherent to the material's physical processes, Auger recombination cannot be avoided [43]

Shockley-Read-Hall (SRH) recombination, which involves trap states in the bandgap, is another kind. Free carriers are "captured" by trap states, which impede their passage through the material. They can be destroyed if the opposite charge is trapped before the first one is released, or they can be released through thermal activation. The traps in the second scenario are referred to as recombination centers. Trap states result from flaws in the semiconductor's crystal lattice. These can be caused, for instance, by thermal cracking, surface states, or a mismatch in the lattice of the layers below, which leads to stress build-up and the creation of dislocations.

I.7. Conclusion

This chapter, a short review of how TPV system works with a brief history showing the TPV conversion in different aspects, The advantage of those systems compared to conventional solar PV systems is that it is possible to control the emission properties of the radiator to increase the performances of the system can lead to acknowledging some of the features proprieties and ideas, We spelled out the essential TPV components, and their diversity such as the used heat sources (blackbodies) in; the spectral control devices, absorber/emitters, and filters then we describe how semiconductor TPV cells can be improved playing on bandgap and all electronic parameters. As the last point, TPVs technologies remain a very attractive renewable field, which should be investigated further. Due to new developments as well as a growing application field for TPV devices, widespread commercialization might occur soon.

Chapter II: An Overview of Metamaterials

II.1 Introduction

This chapter introduces the concepts of electromagnetic Metamaterials (MTMs) with a short historical review, furthermore, they have exceptional optical properties and do not mostly exist in nature such as negative permittivity with a ray of wires (and/or) permeability with split-ring resonators (SRR), and negative refractive index. Therefore, we studied the basic theoretical aspects of electromagnetic wave propagation in matters and their interaction in different materials such as metals and dielectrics which are essential to know the term Plasmonics-based Metamaterials supported in the metals/dielectrics interface which were required in our studies, especially in light trapping configuration, this phenomenon it will be more discussed in Chapter 3.

II.2 History of Metamaterials

Although the word metamaterials (MTMs) was first introduced by Smith in 2000 [44], their earliest application can be traced back to the fourth century AD, when people first used MTMs to decorate pieces of art; for example, the Lycurgus Cup made using ruby glass with gold Nanostructures embedded. In 1898, Bose manufactured a kind of "twisted jute" material consisting of period sub-wavelength meta-atoms with an artificial chiral effect. This is the first significant MTMs structure engineered by modern technology [42]. In the 1940s – 1960s, scientists focused on the interaction between microwave radiation and artificial dielectrics with periodical arrays of metallic plates wires, and spheres [45], [46]**.** In 1968, a milestone paper in electromagnetic MTMs research was published by Veselago [47]. In his paper, Veselago pointed out that the electric field vector (**E**), magnetic field vector (**H**), and wave vector (*k*) formed a left-handed system. Therefore, MTMs were essentially a left-hand material (LHM) that did not obey the right-handed law, like normal materials [47]. Smith made the first demonstration of Veselago's prediction in 2000 [44]. The focus on the engineering uses of metamaterials began in 2000 when Pendry showed that it

was possible to create the alleged "perfect lens" using the special properties of MTMs [48]. The gap between the various novel theories of MTMs and their practical application was filled by Pendry's work. They are synthetic structures related to MTMs that are spread out across split-ring resonators (SRRS). Additionally, they serve to generate the necessary magnetic susceptibility, which is a magnetic response in different MTM types up to 200 terahertz or even higher. These media are capable of producing the strong magnetic coupling required for an applied electromagnetic field (EMF), which is not possible with more traditional materials. By coupling the periodic array and split-ring resonators, for instance, an effect similar to a negative permeability is produced [49].

When an incident wave strikes a metal surface at a frequency that is below or closes to the plasma frequency (ω_p), negative permittivity (ε) results. The incident wave will primarily be reflected from the metal in this scenario because the independent electrons can move up in a way that cancels incident waves (more like a mirror). When the permittivity is positive and the electrons cannot move in a way to cancel the incident wave, the wave will penetrate the metal if the frequency of the incident wave is higher than the plasma frequency [49]. According to negative permittivity, the incident light cancels out because there are enough free electrons to oscillate in the opposite side phase. As a result, the light is blocked from entering.

II.3 Classification of Metamaterials

Figure 2.1 can be used to show how electromagnetic MTMs are classified [50] :

- Double positive (DPS) materials or right-handed MTMs (RHM) are terms used to describe mediums with ($\varepsilon > 0, \mu > 0$), which most dielectrics fall under.

- Epsilon-negative (ENG) mediums or electrical MTMs are defined as mediums with ($\varepsilon < 0$, $\mu > 0$). Numerous electrical plasmas exhibit these properties in specific frequency ranges, including noble metals at optical wavelengths, doped semiconductors in specific frequency ranges below the plasma frequency, and ferroelectric materials.
- Mu-negative (MNG) mediums, also known as magnetic MTMs, are defined as mediums with ($\varepsilon > 0$, $\mu < 0$). Some gyro-tropic or ferrite materials exhibit this property in specific frequency ranges.
- Double-negative (DNG) mediums or left-handed MTMs are terms used to describe mediums with the symbols ($\varepsilon < 0$, $\mu < 0$). (LHM). Only artificial structures have been used to establish this class of media. There is no such substance in nature.
- It is possible to create MTMs with near-zero or zero refractive indices (NZI) when $\varepsilon \approx 0$ or $\mu \approx 0$. Such media also have properties that can be used to realize selective emission and tunneling waveguides, including no spatial phase change and a very large phase velocity [51].

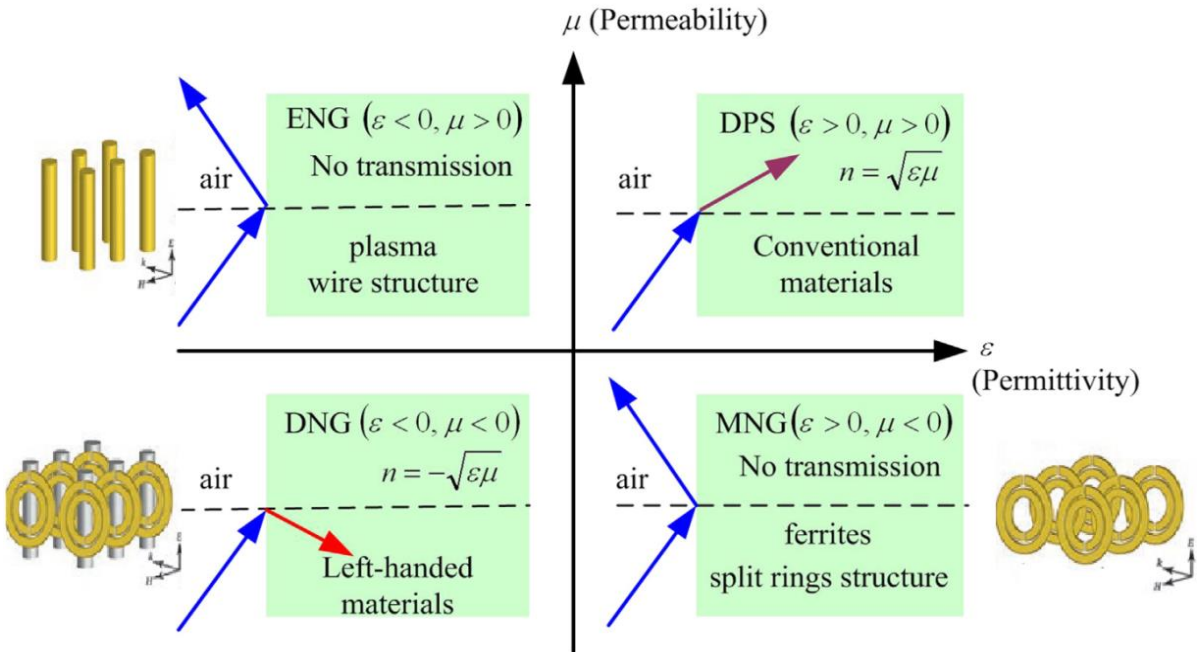

Fig.2. 1: Classification of electromagnetic MTMs based on permeability (μ) and permittivity (ε).

The negative refraction index is caused by the possibility of both negative material permittivity (ε) and permeability (μ) in MTMs. The following formula can be used to calculate the refraction index n [52]:

$$n = \pm\sqrt{\varepsilon_r \mu_r} n = \pm\sqrt{\varepsilon_r \mu_r} \quad \textbf{Eq(2. 1)}$$

Refraction index *n* is consequently negative. The perfect lens and invisible cloak applications, which are both MTMs, are built on this, the most significant and distinctive quality possessed by MTMs. Maxwell's Equations in MTMs can be thoroughly examined to uncover more intriguing properties [52]. The dimensionality of the structures, which form a bulked 3D design with a significant number of constitutive elements oriented in each direction, is another aspect of MTMs classification (x, y, and z). surface (2D) materials, when the structure is a thin film with just one to three constitutive elements distributed evenly across its thickness. Meta-surface (2D) or thin film (2D) MTMs are common names for these MTMs. They are also known as meta-waveguides components, and they are linear (1D) structures that are designed at the nanoscale [50].

II.3.1 Properties of Metals

THz frequencies are now being used for MTM applications instead of radio frequency (RF) and microwave frequencies, and the materials that were used to design these structures have changed in propriety as well. Printed metal (such as copper...) wires on top of printed circuit board material are frequently used to build MTM structures like frequency selective surfaces (FSS) that operate at RF and microwave frequencies. The metal is regarded as an ideal electrical conductor at these

frequencies (PEC). The metal's dielectric properties are assumed to be negligible, and the materials can be thought of as having high electrical conductivity and negligible losses. The movement of free electrons in groups within the metal's crystalline structure is a common contributor to the electromagnetic response of metal. In this scenario, the electrons are taken to be completely free to move wherever they please within the metal, with no restoring force or spring constant. As a result, the resonance frequency predicted by the conventional Lorentz model is zero in this instance and does not manifest itself in the study. The Drude free electron model is used to describe how electrons move through metal. The equation of motion for free electrons in a metal is given by [53] for the note harmonic incident electric field ($E_0.e^{-i\omega t}$):

$$\vec{r}(t) = \frac{e}{m}\frac{e\vec{E}_0 e^{-i\omega t}}{(\omega^2 + i\Gamma\omega)} \qquad \textbf{Eq(2. 2)}$$

Where Γ is the damping constant, *e*, and *m* stand for the charge and effective mass of the electron respectively. By resolving this, we can determine the electron's displacement from its initial position, or r:

$$\varepsilon(\omega) = 1 - \frac{\omega_p^2}{\omega^2 + i.\Gamma\omega} = 1 - \frac{\omega_p^2}{\omega^2 + i.\Gamma^2} + i\frac{\omega_p^2.\Gamma}{\omega.(\omega^2 + \Gamma^2)} \qquad \textbf{Eq(2. 3)}$$

where *p* denotes the frequency of the volume plasma at which the density of the electron gas oscillates [54]:

$$\omega_p = \sqrt{\frac{ne^2}{\varepsilon_0 m}} \qquad \textbf{Eq(2. 4)}$$

In particular, the optical properties of metals are treated elegantly and succinctly by the Drude model, which is intended for the dielectric function of the metallic materials by equation (2.4). To

accurately reflect reality, it must be altered though. It is a well-known fact that gold and silver, which have nearly identical plasma frequencies, appear very differently when exposed to the visible light regime, contrary to what the Drude model predicts [55]. Table 2.1 displays some examples of these.

Metal	$\omega_p(eV)$	$\omega_p(10^{15}s^{-1})$	$\Gamma(eV)$	$\Gamma(10^{15}s^{-1})$
Silver	**9.2**	**14.0**	**0.0021**	**0.032**
Gold	**3.1**	**13.8**	**0.072**	**0.11**
Copper	**8.8**	**13.4**	**0.092**	**0.14**
Aluminum	**15.1**	**22.9**	**0.605**	**0.92**

Table.2. 1: The plasma frequency ω_p, damping constant Γ of selected noble metals [54]

II.3.2 Properties of dielectrics

Over a large portion of the electromagnetic spectrum, MTMs absorbers made of metal, metal-dielectric, or dielectric materials have been realized and have shown novel applications and properties. But because most absorbers are made of metals, which have a low melting point, a high Ohmic loss, and a high thermal conductivity, their use is constrained. All-dielectric metasurface absorbers based on hybrid dielectric waveguide resonances were created to overcome these restrictions. The following Maxwell's equations [52], [5] can be used to examine the fundamental physical background of a wave interacting with a [53]:

$$D = \varepsilon_0 E + P = \varepsilon_0(1+\chi_e)E = \varepsilon_0\varepsilon_r E \qquad \textbf{Eq(2. 5)}$$

$$B = \mu_0 H + M = \mu_0(1+\chi_m)H = \mu_0\mu_r H \qquad \textbf{Eq(2. 6)}$$

E represents the electric field (*V/m*), H the magnetic field (*A/m*), B the magnetic displacement (T or Vs/m^2), and D the electric displacement (C/m^2). Equations provide the electric and magnetic displacements in a homogeneous isotropic medium [56].

$$\vec{D} = \varepsilon \vec{E} \qquad \textbf{Eq(2. 7)}$$

$$\vec{B} = \mu \vec{H} \qquad \textbf{Eq(2. 8)}$$

The relationship between equations (2.5) and (2.6) shows the pair of electric and magnetic displacement ($\vec{D}, H$) with the pair of electric and magnetic field (**E, B**), through a couple of electric and magnetic susceptibilities (χ_e, χ_m), with and, representing the vacuum permittivity and permeability, respectively, through a couple of electric and magnetic polarizabilities (**P, M**). The subscript r in the relative permittivity and permeability will be removed. To determine the solutions of Maxwell's equations using the appropriate boundary conditions is basically how electromagnetic waves interact with any material. As a result, the frequency-domain versions of equations (2.7) and (2.8) can be expressed as [54]:

$$D(\omega) = \varepsilon_0 \varepsilon_r(\omega) E(\omega) = \varepsilon_0 \left[1 + \chi_e(\omega)\right] E(\omega) \qquad \textbf{Eq(2. 9)}$$

$$B(\omega) = \mu_0 \mu_r(\omega) H(\omega) = \mu_0 \left[1 + \chi_m(\omega)\right] H(\omega) \qquad \textbf{Eq(2. 10)}$$

Strongly dispersive MTMs are the norm for metal-dielectric composites [57]. Because metals are much more dispersive than dielectric materials in the infrared or visible wavelength regime, the origin of the dispersion in MTMs is primarily attributed to the metallic component. It is crucial to check that the chosen dielectric constituent is transparent within the targeted wavelength range

when designing an optical-MTM structure. Including the frequency influence of the dielectric function $\varepsilon(\omega)$ in metallic media is also very beneficial.

II.4 Nanostructured Metamaterials enhancement

Nanostructure MTMs, which are an extension of the science of MTMs to the quantum level, have quantum coherent unit elements with desired (engineered) parameters. Additionally, some of these elements' quantum states can be directly controlled, and the system can maintain global coherence for a period of time longer than the traversal time of the relevant electromagnetic signal. These characteristics regulate macroscopic quantum coherence, which transforms a quantum MTM into a qualitatively unique system with several peculiar characteristics and applications [58]. As the two-dimensional equivalent of MTMs, metasurfaces are a significant class of MTMs Nano-structures and have a wide range of applications depending on their constitutive materials and geometry.

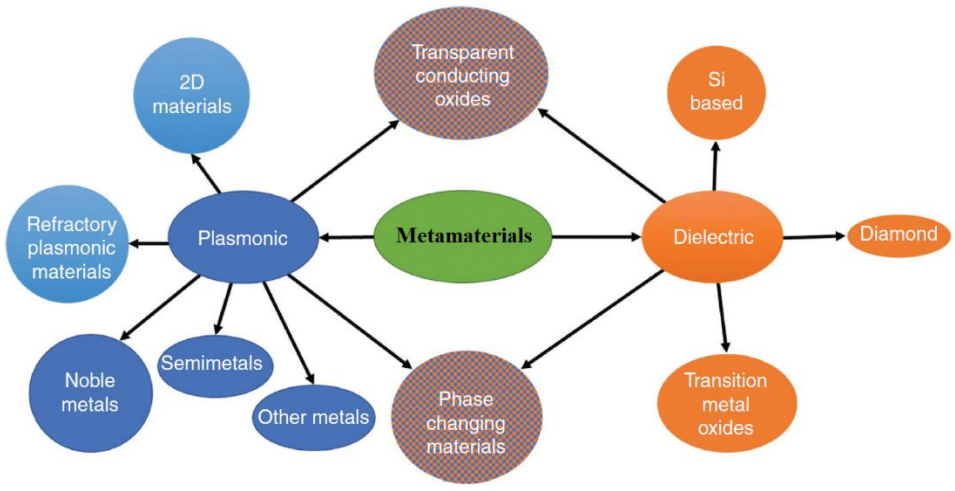

Fig.2. 2: Emerging material platforms for optical MTM including noble and other commonly used in plasmonics metals; semimetals and intermetallic compounds exhibiting metallic behavior (such as metal nitrides, hydrides, oxides, borides, etc.); transparent conducting oxides; and dielectrics [59].

However, based on their frequency responses, all MTM-based devices can be divided into three categories: broadband, wideband, and narrowband [58]. All metasurfaces can be categorized into the two general classes of plasmonic and dielectric metasurfaces, as depicted in Figure 2.2 [60].

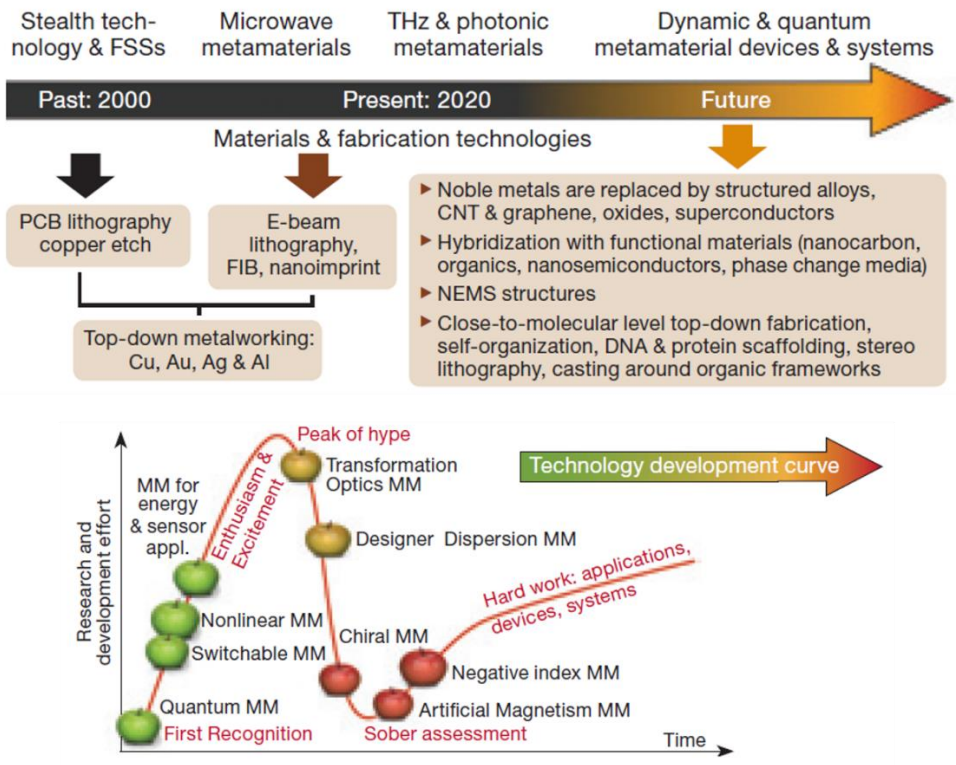

Fig.2. 3: Outlook of the future trends of MTM and meta-devices applications [61].

The research in Meta-surfaces will be centered on a variety of topics in the coming years, as shown in Figure 2.3, including but not limited to [62]. In general, there is a clear tendency to shift the focus of research from the microwave to the optical or the newly emerging THz region. The expansion of the frequency range might seem simple and therefore not have as much physical significance. We must therefore keep in mind that at various frequencies, the properties of the materials themselves would change significantly. There will also be variations in the measurement tools and fabrication processes. When using certain optical frequencies [63].

A Plasmon is an oscillating quantum of free electrons. At the interface between metals and dielectric media, free electron clouds in a metal can couple to light, produce surface plasmons, and deal with the coupling between electronic oscillations and a material's electromagnetic field. Using a metal nanostructure that has been properly designed, At the sub-diffraction scale, surface plasmons may allow for light control. In addition to being able to direct light at the nanoscale, plasmonic nanostructures can also greatly intensify the local electromagnetic field [64]

The incoming radiation's electric field polarizes the conduction electrons in metallic subwavelength structures or Nanostructures. The resulting plasmon oscillations are localized inside the particle and dispersed throughout the Nanostructure volume. Localized surface plasmons are the name given to these plasmon oscillations (LSPs). A restoring force that tries to entice the electrons back into the lattice is created when the electron clouds are expelled from the structure. As a result, the Nanostructures restore the Coulomb force and act as an oscillator driven by the incoming field while also acting as a simple dipole in the direction of the electric field.

Optical losses in plasmonic devices severely restrict the use of plasmonic Meta-surfaces in place of conventional optical elements, despite all the promising applications for them. Heat is produced as a result of the scattering that occurs in the materials as the oscillating electron clouds in the metal interact with the incoming electromagnetic waves. Even though the high plasmonic property, which is a large negative real part of permittivity, and low loss, or we can say a small imaginary part of permittivity, are necessary for the best plasmonic material, the losses cannot be completely avoided. The act of nanostructuring a metal results in the truncation of the magnetic field of an incoming electromagnetic wave as the wave interacts with the free electrons of the structures, even for a perfect plasmonic material with negligible loss. As shown in Table 2.2, the material also has a different platform.

Material type	Examples	Wavelength range	Advantages	Limitations/challenges	Application examples
Plasmonic metal	Au, Ag, Al, Cu...	Visible–mid IR	- Established fabrication - Plasmonic in the UV part of the spectrum (Ag, Al) - Biocompatible (Au) - Small device footprint - High field concentration	Relatively low melting point; - Lack of tunability - High solubility/diffusion at elevated temperature - Low chemical stability (Ag, Al)	- Proof-of-concept demonstrations of compact and flat optical devices - Biosensing (Au) -Structured coloration and holography (Al)
Refractory	TiN, ZrN, HfN, W, Ta…	Visible–mid IR	High durability -High melting point -CMOS compatible -Chemical stability (TiN) -Biocompatible (TiN) -Low solubility -Epitaxially grown -Possibility of growing ultrathin films (few nm)	Higher optical loss in visible compared to noble metals -Strict fabrication requirements	-Local heating and absorbers -High temperature and high intensities -Fabrication of epitaxial Ag (TiN) -Biomedical thermo-plasmonics (TiN)
2D	Graphene, MXene, Phosphorene, MoS2, WSe2, WS2…	Visible–mid IR	-Dynamic tunability (electrical) -Fast modulation -Large field confinement - Compactness/lightweight -Mechanical flexibility -Lower loss than noble metals in near IR	Poor light absorption with single layer	Dynamically tunable and flexible devices
Phase change	GST, VO2, YH2, MgH2, PdH2, SmNiO3	Visible–mid IR	Dynamic tenability (temperature) -Large optical modulation	Relatively slow modulation	Nonvolatile reversible optical switches
Transparent conducting oxides	ITO, Ga:ZnO, Al:ZnO	Visible–mid IR	-ENZ in near IR -Ultrafast tenability (optical, electrical, temperature)	Less plasmonic in the NIR compared to noble metals	Ultrafast optical modulators
Dielectric	Si, TiO2, SiO2, Si3N4, diamond	Visible–Near IR	Very low-optical loss chemical robustness and Mechanical	Larger device footprint Low field confinement	Highly efficient metasurfaces

Table.2. 2:Different material platforms with their wavelength range, advantages, limitations, and applications are described in Ref *[60]*.

II.5 Conclusion

This chapter set out to make a general theory of electromagnetic MTMS and a brief historical review explaining involving MTMS idea in different domains, particularly in developing Plasmonics phenomena, a better understanding of MTMS needs basics of electromagnetic properties that were explained in both cases dielectrics and metals put an appearance of Plasmonics that were discussed alongside with all the plasmonic requirements. In conclusion, we offered a methodology to study and characterize the relevant materials already used for Plasmonics which are deeply have been investigated in the next chapter.

Chapter III: A Plasmonic-based light trapping strategy

III.1. Introduction

In this chapter, we need to expose ways of optical power confinements in subwavelength volumes and find structures to control and light management at the nano-scale. Because their ability to focus is constrained by diffraction, conventional methods of light concentration like dielectric lenses or parabolic mirrors do not offer a possibility of achieving this objective. Other technics are required so that propagating waves can excite oscillations that change in space much more quickly than they do now. Such devices are common in the fields of RF engineering. Using noble metals is one technique that could be used to address these optical problems. Resonant modes at the interfaces between metals ($\varepsilon<0$) and dielectrics ($\varepsilon>0$) can have rather localized distributions of electromagnetic fields in space, even though electromagnetic waves cannot propagate inside bulk pieces of conductors. Can we use metal components to effectively confine electromagnetic fields in the visible and infrared spectra in the same way that metal RF antennas, metal coaxial cables, and small LC resonators do? Plasmonics provides an answer to this query in the current chapter.

III.2. Surface Plasmon Polaritons (SPP)

Surface waves called surface plasmon polaritons (SPP) can travel along metal and dielectric interfaces. The fields exponentially decay away from the interface because they are essentially inhomogeneous plane waves with an imaginary "propagation constant" in the direction orthogonal to the interface. Such a surface-wave structure may potentially function as a waveguide with a subwavelength cross-section size if this decay factor is high and the surface field concentration is strong enough. We might also be able to realize subwavelength field confinement along the surface if the propagation constant on the surface is large enough (much larger than the free-space constant)[65].

III.2.1. Dispersion Equation

We must first introduce some fundamental philosophies about plane waves near planar interfaces to comprehend the characteristics of these surface waves. When we refer to waves in this context, we mean those whose complex amplitudes depend on the position vector *r* as $exp^{(-jk\ r)}$, where *r* may be a complex vector. Evanescent waves, also known as inhomogeneous plane waves, are plane waves in this sense. Let's take a look at plane electromagnetic waves in an isotropic medium near a planar interface with another material or a planar boundary. Since the tangential to the surface (orthogonal to *n*) components of the plane-wave fields are continuous across the interface, it is convenient to introduce a unit vector normal to the interface **n** and consider these components in this scenario. Figure 3.1 illustrates this situation. In the formula $k = k_n\mathbf{n} + k_t$, the wavevector $k = \omega\sqrt{\varepsilon\mu}$ is divided into its normal and tangential components, where kt **n** = *0*. We write the dispersion equation for plane waves where denotes the length of the wavevector.

$$k_n^2 + k_t^2 = k^2 \qquad \textbf{Eq.(3. 1)}$$

Thus

$$k_n = \sqrt{k^2 - k_t^2} \qquad \textbf{Eq.(3. 2)}$$

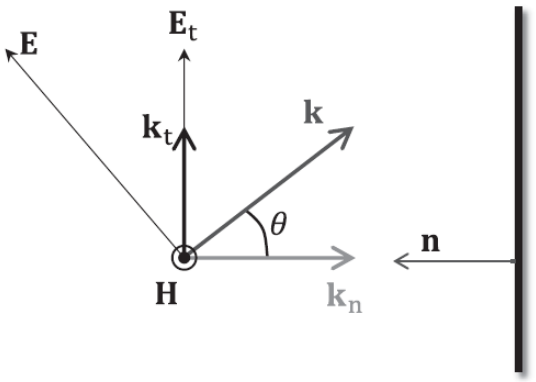

Fig.3. 1: A transverse-magnetic (TM) polarized plane wave in a vicinity of a planar surface, shown by a vertical line.

Because both tangential field components are continuous across the interface, it is convenient to introduce wave impedance as the ratio of the tangential to the interface components of the plane-wave fields. For this example of transverse magnetic (TM) polarized waves, we have[65]:

$$\mathbf{E}_t = \sqrt{\frac{\mu}{\varepsilon}}\cos\theta.\mathbf{n}\times\mathbf{H} = \sqrt{\frac{\mu}{\varepsilon}}\frac{k_n}{k}\mathbf{n}\times\mathbf{H} = \frac{k_n}{\omega\varepsilon}\mathbf{n}\times\mathbf{H} \qquad \textbf{Eq.(3. 3)}$$

In this instance, θ is known as the "incidence angle" and it denotes the angle formed by vector ***k*** and the interface's normal. The dispersion equation for surface waves that travel along an interface and decay normally is now available for us to solve. To satisfy the boundary conditions, which state that the tangential fields must be continuous across the interface, we only need to substitute the corresponding material parameters of the two media. Equations (3.2) and (3.3) hold for plane-wave fields on both sides of the interface. so that we have:

$$\frac{k_{n1}}{\omega\varepsilon_1} = -\frac{k_{n2}}{\omega\varepsilon_2} \qquad \textbf{Eq.(3. 4)}$$

Here, we have taken into account that the unit vector **n** is directed in the opposite direction on the other side of the interface. Assume that the medium on one side has permittivity and is a lossless

metal and that the other half of the space is filled with a lossless isotropic dielectric. The normal component of the wavevector of plane waves on both sides must be imaginary because we are searching for solutions with $|k_t| > |k_{1,2}|$, which would exponentially decay away from the interface (see (Eq. 3.2)). The signs $k_{n1,2}$ should be opposite because waves should decay in both the positive (medium 1) and the negative (medium 2) directions of the unit vector **n**. Therefore, this equation can only have nontrivial surface wave solutions if and have the opposite signs, which is exactly what happens at our interface between lossless dielectric (positive ε) and metal (negative ε). Finding the dispersion equation requires substituting the values of $k_{n1,2}$ from (Eq. 3.2) and solving for the propagation constant's tangential to interface component k_t, we find the dispersion equation:

$$k_t = \omega\sqrt{\mu_0}\sqrt{\frac{\varepsilon_1\varepsilon_2}{\varepsilon_1+\varepsilon_2}} = \omega\sqrt{\varepsilon_0\mu_0}\sqrt{\frac{\varepsilon_{r1}\varepsilon_{r2}}{\varepsilon_{r1}+\varepsilon_{r2}}} \qquad \textbf{Eq.(3. 5)}$$

When permittivities are swapped out for the corresponding permeabilities in the orthogonal (TE) polarization's eigenvalue equation (Eq 3.4). It has no solutions for metal-dielectric interfaces because both permeabilities are positive.

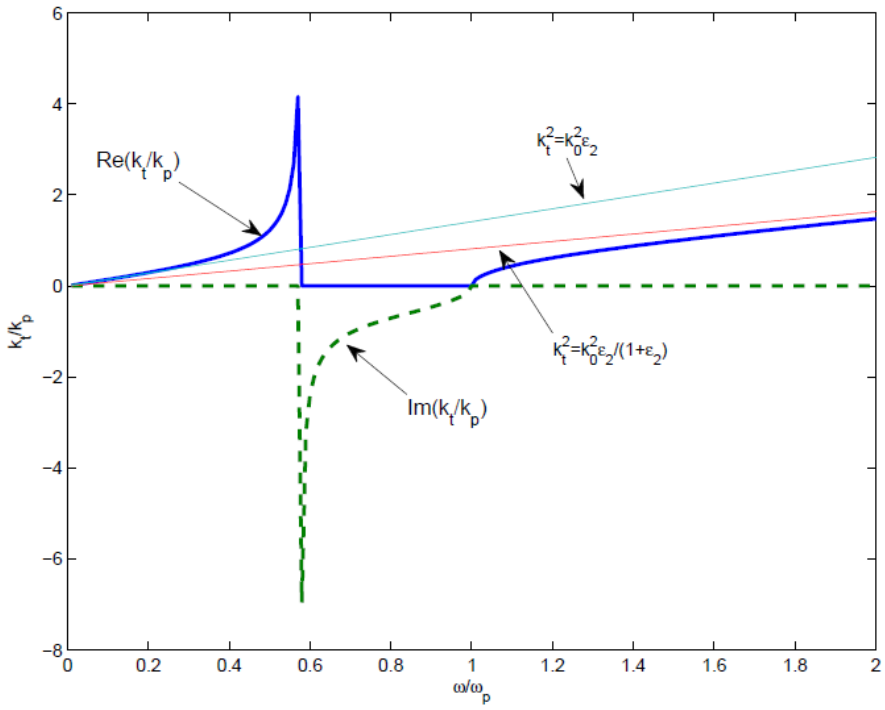

Fig.3. 2: Example of dispersion curves for SPP in the case of negligible absorption. The wavenumbers are normalized to the plasma wavenumber $k_p = \omega_p \sqrt{\varepsilon_0 \mu_0}$. Plot parameters: $\varepsilon_{r2} = 2$, the Drude model for lossless conductors [65].

Figure 3.2 illustrates a dispersion curve example for surface waves at metal-dielectric interfaces without accounting for losses in either medium. The Drude model ($\varepsilon = \varepsilon_0 \left(1 - \frac{\omega_p^2}{\omega^2 - j\omega\nu} \right)$) with a loss factor of zero is used to simulate the dispersion of metal while neglecting the permittivity of the dielectric. The resonance pitch (in some cases called the surface plasmon frequency)[65]:

$$\omega_{SPP} = \omega_p \sqrt{\frac{\varepsilon_0}{\varepsilon_0 + \varepsilon_2}} \qquad \textbf{Eq.(3. 6)}$$

Corresponds to the region where the propagation constant k_t tends to infinity and the denominator of (Eq. 3.5) tends to zero. There is a stop band in the frequency range $\omega_{SPP} < \omega < \omega_P$ (there are no solutions with real values of k_t), and the waves are not surface-bounded at ($\omega < \omega_P$) because the condition $|k_t| > |k_{1,2}|$ | is not met [65]. There is some decay in the passbands and some propagation in the stop band for lossy metals and/or dielectrics because the propagation constant is complex at all frequencies; see an example plot in Figure 3.3.

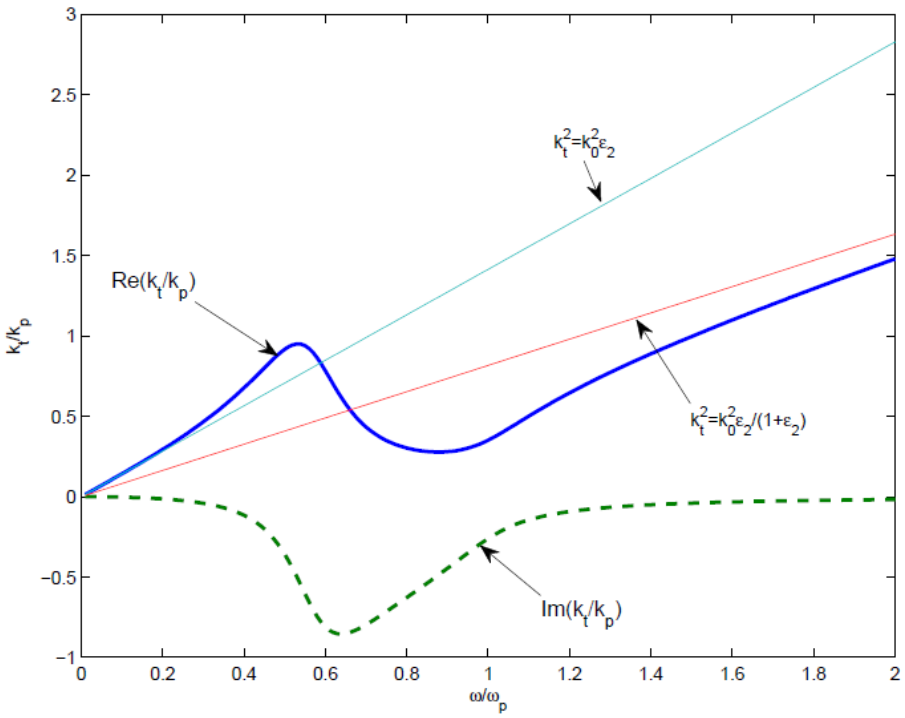

Fig.3. 3: Example of dispersion curves for surface plasmon polaritons: absorptive metal. Plot parameters: $\varepsilon_{r2} = 2$, Drude model for lossy conductors, $\nu/\omega_p = 0.2$ [65].

Due to its relatively low dissipation losses compared to other metals, silver is typically the metal of choice for applications in the visible and infrared ranges. The curves depicted in Figure 3.4 are the results of calculations made using the measured silver permittivity data [65]. As in the earlier examples, the dielectric medium is the same: an unbroken dielectric, We observe that the visible

(roughly 390-700 nm) and infrared spectrums are covered by the surface plasmon polariton, which can propagate in the range from 200 THz (λ_0 = 1.5 μm) to 750 THz (λ_0 = 0.4 m μm= 400 nm) spectra. At various frequencies, the wave's characteristics are very different, though. From the same plot, we can see that the decay rate, which is represented by the imaginary portion of the propagation constant, increases with frequency. Plotting the so-called propagation length, which is equal to the inverse of the imaginary part of the propagation constant: $L = 1/\mathrm{Im}(k_t)$, helps to better visualize it (k_t). In Figure 3.5, this curve is displayed. The propagation length is only a few microns at the high-frequency end of the visible spectrum, whereas, in the infrared range, it can be two orders of magnitude larger than the wavelength.

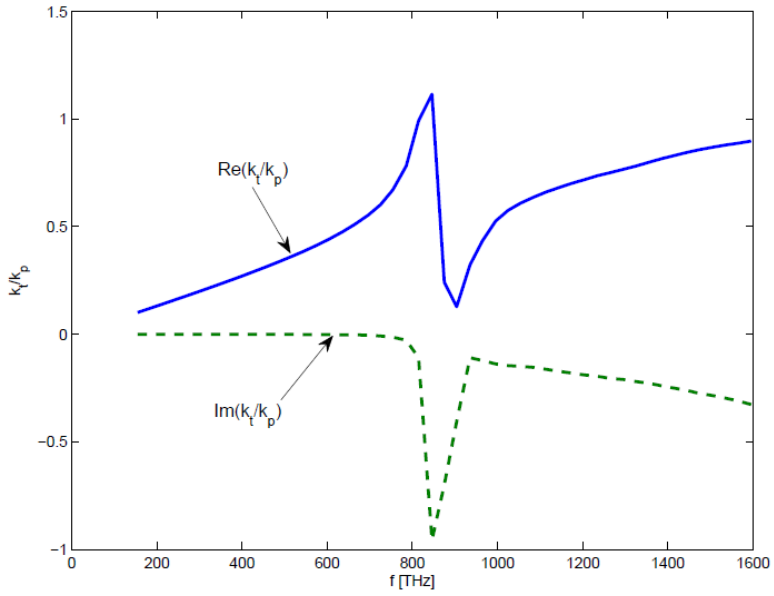

Fig.3. 4 Dispersion curves for surface plasmon polaritons on an interface between silver and a dielectric ($\varepsilon_{r2} = 2$). Experimental data for silver properties [66]. The propagation constant is normalized to the fitting value of the plasma wavenumber, corresponding to the plasma frequency $\omega_p/(2\pi)$=2175*THz* [67].

The confinement of the wave fields to the surface is another crucial factor. After all, the potential to confine the field in subwavelength volumes is one of the primary reasons for using plasmonic structures. In this instance, we seek a waveguiding structure with a cross-sectional area that is

small to the wavelength. The field decay rate in directions normal to the surface, or the inverse values of the normal component of the propagation constant, is used to measure the field confinement (it's imaginary part). In Figure 3.6, the corresponding plots are displayed. We observe that while the fields extend fairly far into the dielectric, especially at low frequencies, they decay relatively quickly into the silver volume. Actually, at the appropriate frequency, the "width" of the plasmonic waveguide is comparable to the free-space wavelength.

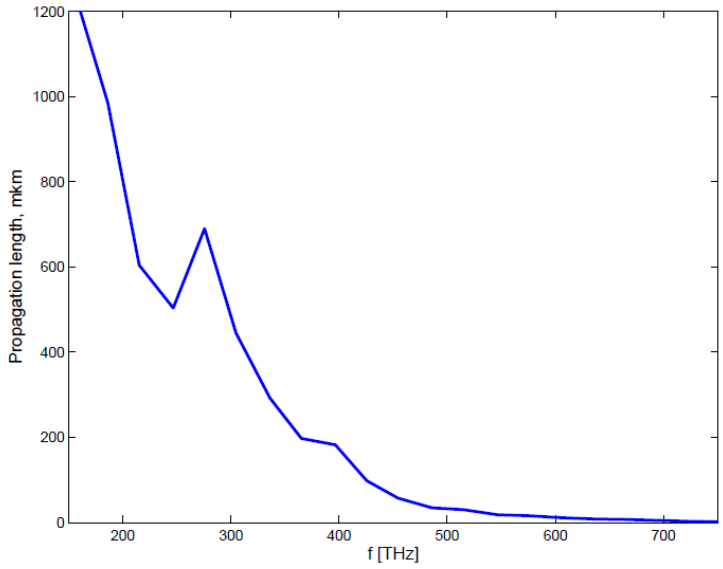

Fig.3. 5 Propagation length L (nm) of SPP on an interface between silver and a dielectric ($\varepsilon_2 = 2$). Experimental data for silver properties [66].

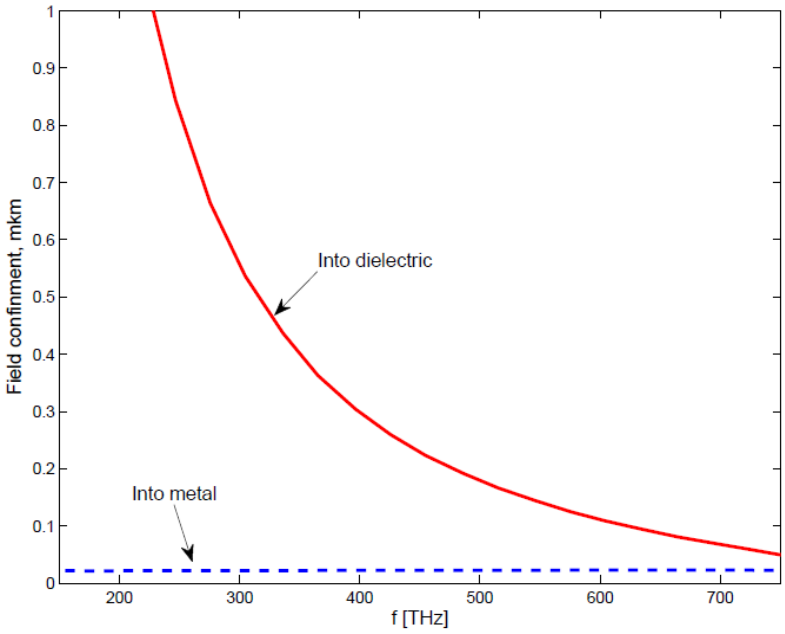

Fig.3. 6 Confinement of fields of surface plasmon polaritons on an interface between silver and a dielectric ($\varepsilon_{r2} = 2$). Experimental data for silver properties [66]

III.2.2. Excitation of SPP modes

Surface waves between two media with wavenumbers $k_{1,2}$ are bound to the surface because the propagation constant along the interface, $|k_t| > |k_{1,2}|$, is greater than the wavenumbers in both media. It means that such waves cannot be excited by propagating plane waves incident on the interface because the exiting wave must be in phase synchronism with the surface wave and the propagating wave's tangential component is always shorter than the length of the wavevector $k_{1,2}$. To convert fields whose variations in space propagate plane waves into fields with quick enough variations in space, a coupling device is required [65].

Using a prism in the full-internal-reflection regime is one option. Due to the continuity of the tangential field components, when a plane wave traveling inside a prism material is fully reflected from one of the prism faces, the field outside the prism is not zero but instead decays exponentially

away from the prism (because all the incident energy is reflected). Because the tangential component of the propagation constant is larger than the length of the wavevector in the medium outside the prism, it is obvious that this exponentially decaying field is a surface wave. Thus, phase synchronism with the eigenwave of the interface mode is made possible by placing such a prism close to an interface that supports SPP modes.

Utilizing a periodic structure is an additional choice (grating). Think about a dielectric/metal interface that permits surface plasmons once more. The surface mode between the dielectric and metal will be an infinite series of Floquet harmonics with the wavenumbers if we periodically perturb the dielectric surface, such as by creating small parallel groves [65].

$$k_{tn} = k_t + n\frac{2\pi}{D} \qquad \textbf{Eq.(3. 7)}$$

where D is the perturbation period, and n =± 1, 2,... It is possible to choose the period so that one of these harmonics propagates in phase with the incident plane wave, i.e., k_{tn} equals the tangential wavevector of the incident propagating plane wave.

Furthermore, the coupling can be achieved by putting one or more tiny particles close to the interface that is home to the surface plasmon polaritons. The particle must either be much smaller than the wavelength of the surrounding space or exhibit subwavelength-scale shape or material inhomogeneities. The spatial variations of fields are quick in the immediate vicinity of subwavelength inhomogeneities, making coupling to plasmon waves with wavelengths smaller than those of propagating waves possible. It can also be understood from the perspective of the Fourier integral expansion of fields near a tiny inhomogeneity. The Fourier spectrum must have large wavenumber plane-wave components that can synchronize with the surface mode to resolve the fine spatial structure of the fields. Metal or dielectric Nanostructures or the tips of near-field

scanning microscopes are typical examples of such couplers. Any surface inhomogeneity serves as a coupler between surface modes and waves that are propagating. Another illustration is the excitation of surface waves at surfaces of finite size by wave propagation illumination of the surface edge [65].

III.3. Plasmonic Applications

Resonant phenomena in optically tiny metal Nanostructures can be used for a wide range of purposes, primarily by taking advantage of opportunities to focus and resonantly strengthen electromagnetic fields in optically tiny regions. The capacity to direct light along plasmonic structures is also useful.

Let's run down the principal application fields [68]:

- Optical circuits (meta-Tronics);
- Enhanced emission, fluorescence, and nonlinearities;
- Enhanced solar cells;
- Metamaterials, including superlenses;
- Nanolasers;
- Applications in biology and medicine (mainly in sensors);

The main practical problem: high dissipation losses in resonant metal Nanostructures or in resonant surface modes.

III.4. Plasmonic light trapping configuration

The purpose of light trapping in thin film solar cells, the special qualities of plasmonic resonances can be utilized by [69]:

1. **Near-field improvement**, Nanostructures (NSs) can serve as an antenna for the incoming light, concentrating the optical energy in the nearby electric field of the surface plasmon mode (near-field confinement), as schematically depicted in Fig. 3.7A. However, for the energy conversion to be effectient, the semiconductor's absorption rate must be greater than the plasmon decay time's reciprocal (typical lifetimes from 10 to 50 fs). This method is especially well suited for some materials, such as organic semiconductors, where it has been shown to increase efficiency by a factor of (1.7), and where small carrier diffusion lengths necessitate ultrathin absorbers for the effective collection of photocarriers [70].
2. **Surface plasmon resonance (SPRs)** are depicted in Fig. 3.7B. Using metallic gratings in the rear mirror, the incident light can be coupled into electromagnetic waves that are traveling along the interface between the metal back contact and the absorber layer. Notably, the incoming light could be effectively turned 90 degrees in this configuration and absorbed along the lateral direction of the solar cell. If only its absorption coefficient were high enough to outweigh the losses in metal, the semiconductor would be able to absorb the majority of the energy due to the evanescent fields' greater penetration depth into it than into the metal. However, SPPs experience relatively high ohmic losses in the visible and near-infrared (NIR) spectral ranges, which shorten propagation times and subsequently restrict their use in solar cells [Chapter 8][69].
3. **Far-field scattering,** Figure 3.7C and D, which depicts far-field scattering. Due to the Localised surface plasmon resonance (LSPR), metallic NSs grating can scatter light effectively over a wide range of solar spectrum wavelengths. Additionally, scattering occurs preferentially in the substance with a higher refractive index when NSs are placed close to the interface between two different dielectrics. As a result of being redirected away

from the specular direction, this scattered light has a longer path than it would otherwise have because its wavelength is not well absorbed by the photovoltaic material. Additionally, light that is scattered at angles greater than the critical angle for total internal reflection (θ_c, which for the Si/air interface is approximately 16 degrees) may be coupled into the guided mode and remain trapped inside the semiconductor slab. The far-field scattering-based light-trapping technique has received the most attention in the last ten years and is considered the most promising for photovoltaic applications [69].

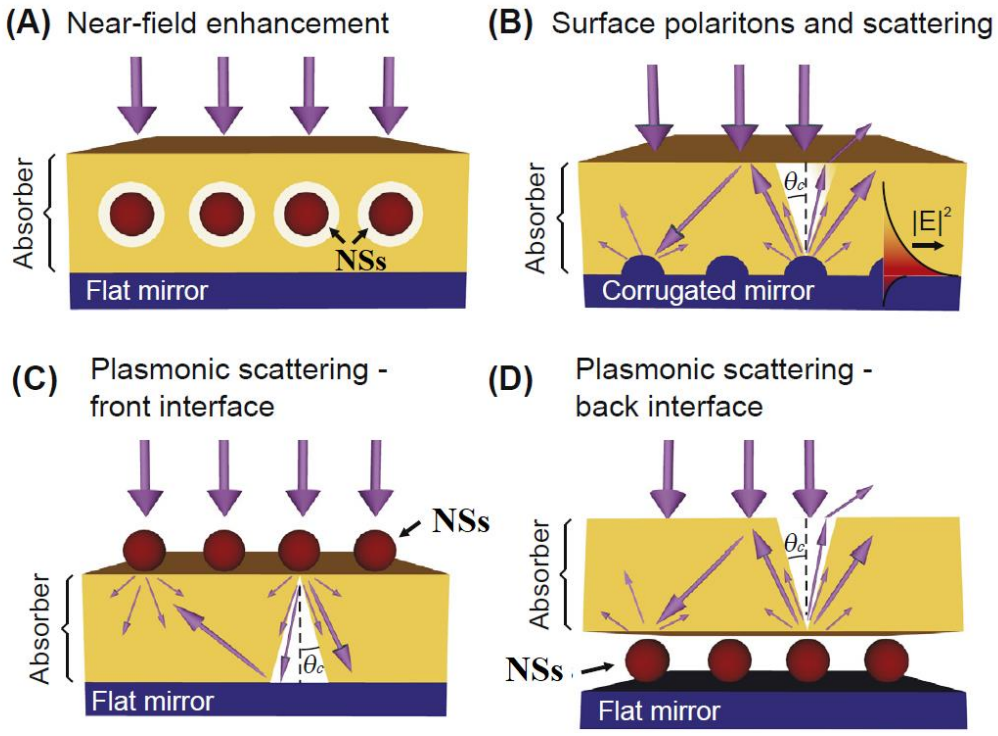

Fig.3. 7 Schematic illustration of plasmon-induced light trapping in thin film solar cells due to **(A)** near-field enhancement**, (B)** surface plasmon polariton and plasmonic scattering provided by corrugated back metallic mirror, and (**C** and **D**) far-field scattering from metallic Nanostructures placed either on the front **(C)** or on the rear **(D)** side of the cell [69].

III.5 Optimization guidelines

The size shape and environment of plasmonic NS gratings have a significant impact on the scattering and absorption of light phenomena. C_{Scatt}(C_{Abs}) is a quantity with area dimensions determined by the ratio of the scattered (absorbed) energy to the incident irradiance [71], which determines how much light is scattered (absorbed) by it. In the literature on single-particle scattering, however, it is more usual to represent the dimensionless scattering (absorption) efficiency [69].

Q_{Scatt} (Q_{Abs}), which is the proportion of C_{Scatt}(C_{Abs}) to the particle cross-sectional area:

$$Q_{Scatt} = \frac{C_{Scatt}}{A} \quad ; \; Q_{Abs} = \frac{C_{Abs}}{A} \qquad \textbf{Eq.(3. 8)}$$

The total of the scattering and absorption efficiencies is the extinction efficiency (Q_{Ext}):

$$Q_{Ext} = Q_{Scatt} + Q_{Abs} \qquad \textbf{Eq.(3. 9)}$$

Theoretical considerations and computational studies published in the literature can be used to derive some optimization recommendations regarding the geometry of NS gratings and device configuration.

- **Size:** Both C_{Scatt} and Q_{Scatt} increase rapidly with the growing NS gratings diameter up to 100 nm. In addition, the spectral position of LSPR changes toward longer wavelengths and broadens significantly [72], [73]. Hence, for solar cell applications, big NS gratings, with sizes of 100 - 200 *nm* are generally a better choice. On the other hand, bigger NS gratings may shift the dipolar resonance.

- **Shape:** The cross-sectional shape of the grating determines their spectral response as well as the efficiency of light trapping into the photovoltaic and thermophotovoltaic material because the light is preferentially confined or/and scattered toward the material with a high refractive index. Hence, the most required are geometries with high contact area to the substrate, i.e., cylinder or hemisphere [74].
- **Environment:** High refractive index of the embedding medium is beneficial for the redshift of LSPR. In addition, when the NS gratings are set close to the interface between two dielectric materials, a strong preferential scattering toward the high-refractive-index material occurs. Therefore, for rear-located gratings, the coupling efficiency increases significantly with decreasing spacing layer between Si and the NSs, which has been demonstrated experimentally [75], and theoretically [76], and can be explained by an overlap between NS near field and the substrate.
- **Device configuration:** The high optical losses in the NS gratings at short wavelengths can be stopped by placing them on the rear side so that they interact only with long wavelength photons, which are not absorbed during the first pass through the absorber material [75], [77]. Such configuration has been widely studied, resulting in the experimental demonstration of high photogenerated currents; for instance, 16.9 and 21 mA/cm^2 have been achieved as the result of light trapping provided by a nanopatterned back reflector (BR) in ultrathin a-Si:H [78], and mc-Si:H photovoltaic cells [79], respectively. The nanopatterning is done, however, with complicated and expensive techniques, like electron beam or nanoimprint lithography. An alternative approach takes

advantage of self-assembled NSs fabricated in the PBR. It has been demonstrated that PBR can provide efficient light trapping, comparable to state-of-the-art random texturing [80], resulting in photocurrents of 15.6 mA/cm^2 achieved with a-Si:H solar cell [81] and 25.5 mA/cm^2 with mc-Si:H [82].

III.6 conclusion

The recent advancements in plasmonics for PV and TPV are summarized in this chapter. For the development of ultra-thin-film PV cells, advanced light-trapping techniques are key to obtaining higher efficiency at lower costs. In this chapter, we summarize the relevant knowledge that can be extracted to unveil plasmonic processes and mechanisms. It is important to understand that electrical parameters should be studied in conjunction with photophysics to ensure that the improvement of plasmonic absorption leads to enhanced efficiency of charges and device performance. Nanostructures, when incorporated into PV devices, enhance antireflection, optical absorption, and wavelength spectrum and help in successful excitons dissociation. Moreover, it has been shown that the plasmonic effect is highly dependent on the distance between the nanostructures and the surface of the absorption layer. Furthermore, the positioning of nanostructures inside or between different layers in PV devices impacts device performance because of the different mechanisms induced. in the next chapter a trapping light in the subwavelength region, nanostructures with specific sizes and geometries are anticipated to obtain the maximum possible thermophotovoltaic conversion efficiency has been investigated.

Chapter IV: Modeling of the Plasmonic light-trapping ultrathin GaSb TPV cell

IV.1 Introduction

In this chapter, we will present the common mathematic approaches used for electromagnetic and optical 3D simulation as well as the mainly used software for that. Afterward, we will extract the optical proprieties of the design under study such as absorption and reflection spectra in different polarization and incident angle sensibility, the results can be validated by the original simulation approved by referred paper. the geometric parameters effect, with the absorbed power per layer, will be discussed also. Furthermore, the TPV efficiency has been calculated as well as the electrical parameters that have been described and computed under different blackbody source temperatures.

IV.2 Numerical methods for plasmonic structures

For modeling a Plasmonic structure, several approaches are available, such as rigorous coupled-wave algorithm (RCWA), finite-difference time-domain method (FDTD), Transmission Line Method (TLM), finite-element method (FEM), method of moment (MoM) and others. Usually, the computational electromagnetic approaches can be classified into either frequency-domain simulation or time-domain simulation [83].

One of the most favorite methods for Metamaterials and Plasmonics problems is the FDTD method proposed by Yee in 1966 [84]. Due to its simplicity, this approach is very popular in the electromagnetic field, and it is especially useful for broadband simulations since one single simulation can cover a wide range of frequencies [53]. However, the FDTD method has a major disadvantage when it is used for complex geometry simulation. In this case, according to the best references of the FEM method Jian's [53], and Peter's Books [85], which have focused on how to develop and implement FEMs for solving Maxwell's equations, the FEM is a better choice as evidenced by several published papers and books in this way.

IV.2.1 Transmission Line Method (TLM)

At an unchanging frequency, the equations are solved in the plane perpendicular to the surface for a given propagation depth through the electromagnetic structure. The field is then transferred during the modeled structure by successively applying Maxwell's Equations to obtain the scattering matrix for a simple layer of electromagnetic structure, and then by cascading the scattering matrix for each structure, the transmission and reflection coefficients can be propagated down through layers of the overall structure by successive matrix multiplication [53].

IV.2.2 Finite-Difference Time-Domain Method (FDTD)

This technique is a time-stepping approach that models how electromagnetic waves in reality travel through an electromagnetic structure. The FDTD method has several different algorithms; however, the most well-structured is the highly accurate algorithm introduced by Kane Yee [86] and was first made commercially available by panoramic technology in 1999. Using the Yee technique, the electromagnetic structure to be simulated is first broken up into a rectangular grid, with the corresponding ε and μ calculated at each spatial position. This algorithm solves the electric and magnetic fields in space and time by utilizing Maxwell's curl equations. By combining Maxwell-Faraday and Maxwell-Ampere equations with the constitutive equations for the electric flux density, and magnetic flux density [53]:

$$\vec{D} = \varepsilon_0 \varepsilon_r \vec{E} \qquad \textbf{Eq (4. 1)}$$

$$\vec{B} = \varepsilon_0 \varepsilon_r \vec{H} \qquad \textbf{Eq (4. 2)}$$

Along with the fact that the electric and magnetic current densities can serve as additional sources of electric (J_{source}) and magnetic (M_{source}) energy [53]:

$$\vec{J} = \vec{J}_{source} + \sigma_E \vec{E} \qquad \textbf{Eq(4. 3)}$$

$$\vec{M} = \vec{M}_{source} + \sigma_E \vec{H} \qquad \textbf{Eq(4. 4)}$$

where σ_E is the electrical conductivity and σ_H is the magnetic loss, we appear at Maxwell's curl equations for linear, isotropic, non-dispersive materials:

$$\frac{\partial \vec{H}}{\partial t} = -\frac{1}{\mu}\nabla \times \vec{E} - \frac{1}{\mu}\left(\vec{M}_{source} + \sigma_H \vec{H}\right) \qquad \textbf{Eq (4. 5)}$$

$$\frac{\partial \vec{E}}{\partial t} = -\frac{1}{\varepsilon}\nabla \times \vec{H} - \frac{1}{\varepsilon}\left(\vec{J}_{source} + \sigma_E \vec{E}\right) \qquad \textbf{Eq (4. 6)}$$

This produces a set of six coupled scalar equations $\partial H_{x,y,z} / \partial t$, $\partial E_{x,y,z} / \partial t$ that represent a "*Yee* cell," in Fig 4.1, where every electric-field component is surrounded by four circulating magnetic-field components and every magnetic-field component is surrounded by four circulating electric-field components. The simulation volume is then extended by an array of Faraday's law and Ampere's law contours. Thus, the method accurately simulates both the differential and integral forms of Maxwell's equations at all the points in the simulation volume [53].

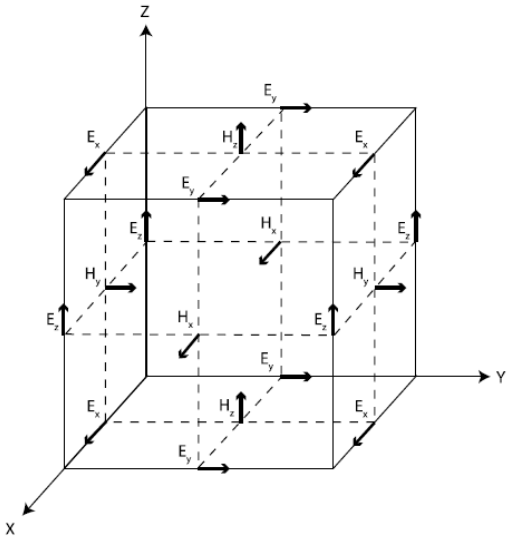

*Fig.4. 1***:** The distribution of electric and magnetic field vector components in the rectangular Yee cell *[87]*.

To calculate each **E** and **H** component at time *t* and position (*x, y, z*), the curl equations are discretized in time, and the electromagnetic field propagates through the simulation volume by exceeding from $E_{x,y,z}(x, y, z, t = 0)$ to $E_{x,y,z}(x+1, y+1, z+1, t = \Delta t)$, and so on. Finally, a Fourier transform of these results yields the field magnitudes and phases at every point and every frequency [53].

IV.2.3 Finite Element Method (FEM)

Compared with the FDTD, the Finite Element Method (FEM) is an originally more complex and universal method. This approach is a numerical process to find accurate and stable solutions to boundary-value partial differential equations [88]. The first time was reported in 1943 by Richard Courant in his work on elasticity and structural analysis, where the concept of mesh procedure of a simulation was introduced. It was not until 1969 that the method was introduced to the field of electromagnetic engineering after Silvester used this approach in the field of microwave engineering [89]. FEM assumes that the resonant structure is surrounded by an artificial absorbing

boundary condition that approximates the electric and magnetic fields approaching zero at infinity [69], [53]:

$$\hat{n}\times(\nabla\times E)-ik_0\hat{n}\times\hat{n}\times E\approx 0 \qquad \textbf{Eq(4. 7)}$$

$$\hat{n}\times(\nabla\times H)-ik_0\hat{n}\times\hat{n}\times H\approx 0 \qquad \textbf{Eq (4. 8)}$$

Following the treatment by *Jin* and *Riley* [53], the boundary conditions in equations (4.7) and (4.8) are combined with the vector wave equation for the electric field of Maxwell's equations:

$$\nabla\times(\frac{\mu_0}{\mu_{ij}}.\nabla\times E)-k_0^2\varepsilon_{ij}E=-ik_0\sqrt{\frac{\mu_0}{\varepsilon_0}}J-\nabla\times\frac{\mu_0}{\mu_{ij}}.M \qquad \textbf{Eq (4. 9)}$$

where *M, and J* are the magnetic and electric current densities, respectively. We arrive at [[1]]:

$$\iiint_V\left[(\nabla\times T).\frac{\mu_0}{\mu_{ij}}.(\nabla\times E)-k_0^2T.\varepsilon_{ij}.E\right]dV=$$
$$\oiint_{S_B\cup S_{surf}}\hat{n}.\left[(T\times\frac{\mu_0}{\mu_{ij}}.\nabla\times E)\right]dS-\iiint_V T.ik_0\left[\sqrt{\frac{\mu_0}{\varepsilon_0}}.J+\nabla\left(\frac{\mu_0}{\mu_{ij}}.M\right)\right]dV \qquad \textbf{Eq(4. 10)}$$

where *V* depicted the total volume of integration, S_B is the artificial absorbing boundary surface, S_{surf} is the surface of the structure being simulated, and T is an appropriate test function used for integration convergence. The combining of the latest four equations offers:

$$\iiint_V\left[(\nabla\times T).\frac{\mu_0}{\mu_{ij}}.(\nabla\times E)-k_0^2T.\varepsilon_{ij}.E\right]dV=$$
$$\oiint_{S_{surf}}(\hat{n}\times T).\frac{\mu_0}{\mu_{ij}}.(\nabla\times E)\;dS-ik_0\oiint_{S_B}(\hat{n}\times T).(\hat{n}\times E)\;dS- \qquad \textbf{Eq (4. 11)}$$
$$\iiint_V T.\left[ik_0\sqrt{\frac{\mu_0}{\varepsilon_0}}J+\nabla\times(\frac{\mu_0}{\mu_{ij}}.M)\right]dV.$$

The volume *V* has then meshed into sub-regions using trapezoidal, tetrahedral, or other types of meshing formats, where the conformal nature of these meshes is especially useful with curvature

surfaces. To get a solution to the electromagnetic problem suggested in equation (4.11), the E-field tangent to each edge of an individual meshing cell is calculated, and a set of basis vectors are used to extrapolate the resulting fields throughout the remaining simulation volume. The E-field within the entire structure is then given by:

$$E = \sum_{k=1}^{R_{\max}} R_k E_k \qquad \textbf{Eq (4. 12)}$$

where R is the vector field component along a given meshing cell edge, $R_{\max}$ is the total number of edges within the simulation except S_{surf}, and E_k is the tangential electric field component along the same edge. When the basis vectors, R are the same as those in the test function T, we can combine equations (4.11) and (4.12) to find the discretized, Galerkin formulation of the electromagnetic problem for a single frequency:

$$\sum_{k=1}^{R_{\max}} M_{kh} E_k = -\iiint_V R_h . \left[ik_0 \sqrt{\frac{\mu_0}{\varepsilon_0}} J + \nabla \times \left(\frac{\mu_0}{\mu_{ij}} . M \right) \right] dV \qquad \textbf{Eq (4. 13)}$$

where M_{kh} is given by:

$$M_{kh} = \iiint_V \left[(\nabla \times R_h) . \frac{\mu_0}{\mu_{ij}} . (\nabla \times R_k) - k_0^2 R_h . \varepsilon_{ij} R_k \right] dV - ik_0 \oiint_{S_B} (\hat{n} \times R_h) . (\hat{n} \times R_k) \, dS \qquad \textbf{Eq (4. 14)}$$

IV.3 3D optical simulator software

There exist several commercially available software that can easily deal with the analysis and simulation of 3D optical design and associated structures as well as general periodic structures, such as High-Frequency Structure Simulation (HFSS) by ANSYS based on FEM method solver, with helpful adaptive mesh refinement, and integrated electromagnetic simulation software (IE3D) by Zeeland software, with the software package (FEKO) The name is derived from the German

acronym "FEldberechnungfür Körpermitbeliebiger Oberfläche", which are based on moment method, and the computer simulation technology CST MICROWAVE STUDIO which is based on three rigorous methods such as FDTD, FEM and TLM approaches, and multi-physics COMSOL based on FEM approach.

In this work, we select the FEM and FDTD approach which is offered by the software CST MICROWAVE STUDIO, The available numerical methods within CST STUDIO SUITE include FDTD, TLM, and FEM [90]. In many cases, it is beneficial to use different approaches for the same problem. The comparison of the results yields an additional validity check for your numerical results. We note that this is not a time-consuming task. In contrast to the use of different software tools for validation, you can use different solver methods in the same CST software without setting up your computational model again [90].

IV.4 Design of Plasmonic light-trapping ultrathin GaSb TPV cell

Figure 4.2 depicts the periodic ultrathin TPV cell-coupled metamaterial structure under study, it has been suggested and numerically investigated in a new study (2018) offered by Qing et al from the School for Engineering of Matter, Transport and Energy Laboratory, Arizona State University, USA [91], which is made of a nanostructured silver (Ag) grating on a Gallium antimonide (GaSb) active layer and Ag back reflector. The Ag grating has a thickness of h = 30 *nm*, period of A = 200 *nm*, and width of w=100*nm*, while the thickness of the GaSb spacer is d = 30*nm*. Note that the bottom Ag back reflector could be as thin as 100*nm* to be opaque in the visible and near-infrared regions. The rigorous coupled-wave algorithm (RCWA) method has been used by this research team to simulate the optical properties of the ultrathin TPV cell-coupled Metamaterial structure shown in Fig. 4.2. RCWA, FEM, FDTD, and TLM are widely used methods to extract the optical properties of nanostructured devices [92], which previously discussed. Based on Floquet's

theorem, the methods solve the solutions of periodic differential equations expanded with Bloch waves. The dielectric function of Ag, ε_{Ag}, is given by a Drude model [93]:

$$\varepsilon_{Ag} = \varepsilon_{\infty} - \frac{\omega_p^2}{\omega^2 + i\omega\Gamma,} \qquad \textbf{Eq(4. 15)}$$

where $\varepsilon_{\infty} = 3.7$ is the infrared dielectric constant, $\varepsilon_P = 9.2eV$ is the unscreened plasma frequency, and $\Gamma = 0.02$ eV is the damping coefficient at room temperature. The optical properties of GaSb were taken from Ref [94].

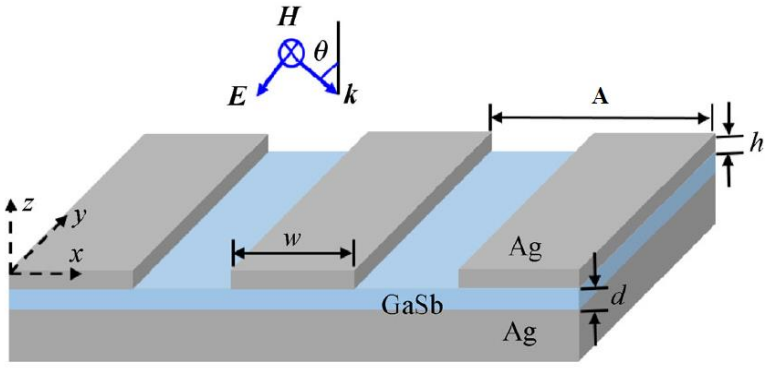

Fig.4. 2*:* Schematic of the ultrathin TPV cell-coupled metamaterial structure under study with three layers of nanostructured Ag grating, ultrathin GaSb layer, and Ag back reflector layer [91]

IV.5.1Simulation outcomes

IV.5.1.1 Absorbance spectra at normal incidence

CST MICROWAVE STUDIO SUITE software offers a variety of meshes and algorithm solvers, which also benefits in an easy possibility of cross-verification of methods and meshes in the same

design. The mesh influences the accuracy and speed of our simulation, so it is worth spending some time understanding the meshing process [90]. The available numerical methods within CST STUDIO SUITE include FDTD, TLM, FEM, and moment method (MoM), by using different mesh types, for example, FDTD and TLM: performs by hexahedral mesh, FEM: performs by tetrahedral mesh, planar MoM: performs by surface mesh. In many cases, it is beneficial to use different meshes for the same optical design. The comparison of the results yields an additional validity check for your numerical results. Note that this is not a time-consuming task. In contrast to the use of different software tools for validation, you can use different solver methods in the same CST software without setting up your computational model again, and this is what we will accomplish in the current section [90]. The spectral of normal absorptance of the Plasmonic light-trapping TPV cell design was calculated under transverse magnetic (TM) and transverse electric (TE) incident waves, as shown in Figure. 4.3. a and b.

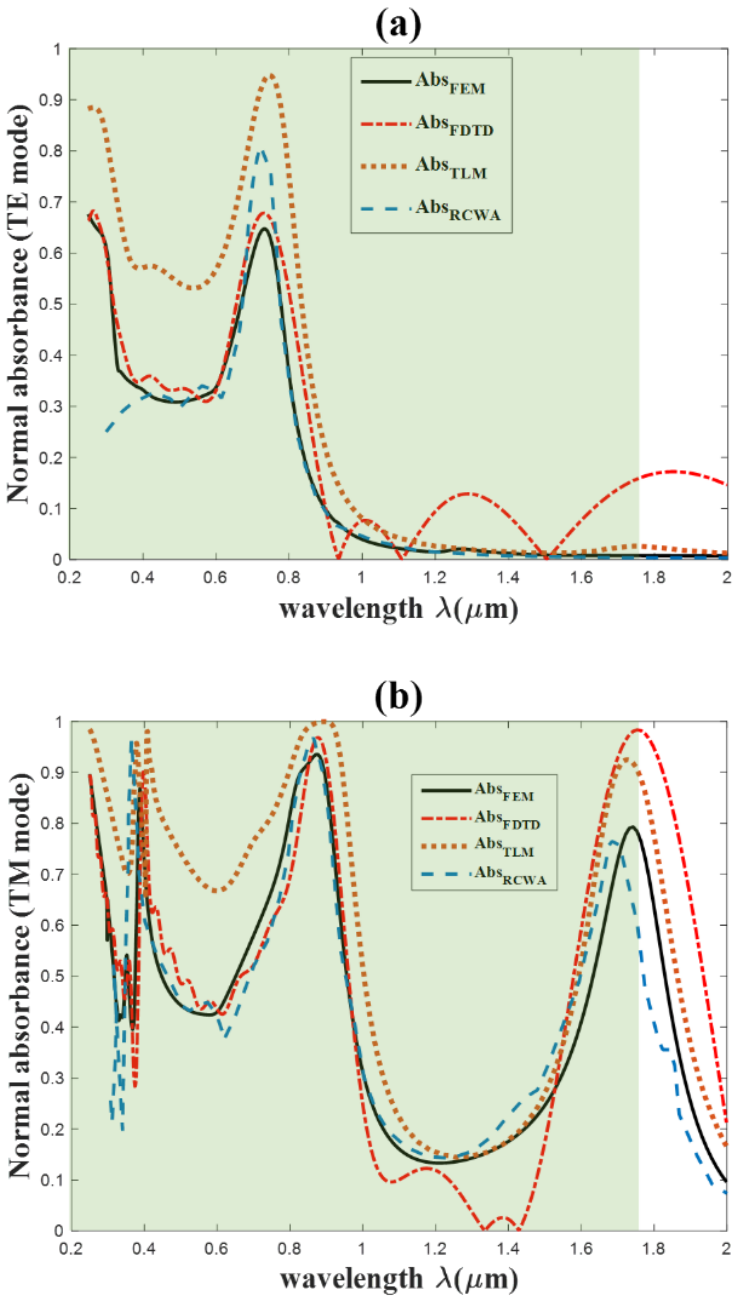

Fig.4. 3: Simulated absorbance spectra for the Plasmonic light-trapping TPV design using CST MICROWAVE STUDIO, compared to the RCWA approach spectra [91]. **(a)** TE mode and **(b)** TM mode polarizations.

The green region represents the useful photon region above the GaSb bandgap ($E_{ph}>E_g$). The computed FEM, FDTD, and TLM absorbance spectra exhibited a good agreement between them and also with the numerical absorbance spectra simulated by the RCWA approach applied by Qing

et al [91]. It is observed that there are three major absorption peaks (α = 0.85 at λ = 0.35 μm , α = 0.78 at λ = 1.74 μm , and α = 0.93at λ = 0.87 μm) under TM incident waves, while there is only one major absorption peak (α = 0.63 at λ = 0.73 μm) under TE incident waves. All the absorption peaks are above the bandgap of GaSb and thus could efficiently enhance the light absorption for photon-generated carriers. It is important to understand the physical mechanisms that are responsible for enhanced light absorption in the ultrathin TPV cell-coupled MTM structure.

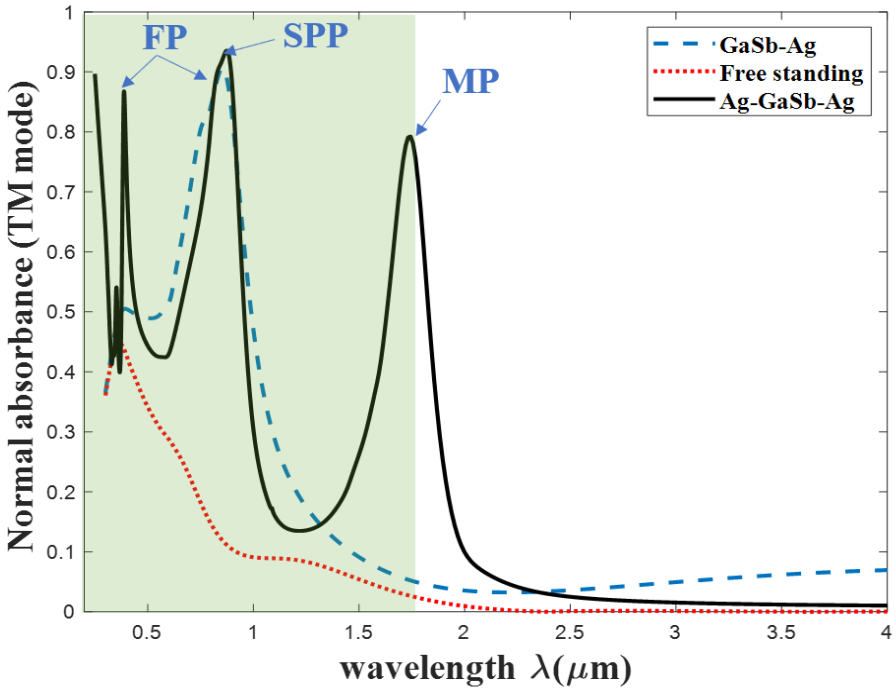

Fig.4. 4: Comparison of normal absorptance between different samples including the ultrathin TPV cell-coupled MTM structure, a GaSb-on-Ag structure, and a free-standing GaSb under TM waves.

Figure 4. 4 compares the normal absorptance of three configurations structures under normal TM incident waves; the first: is an ultrathin TPV cell-coupled MTM structure, the second is a GaSb-Ag structure, and the third is a free-standing GaSb layer. All configurations have a 30 *nm* of GaSb

active layer. It is found that without the upper nanostructured Ag grating, the absorption peak at $\lambda = 1.75\ \mu m$ as well as the peak at $\lambda = 0.35 \mu m$ disappears, while the peak at $\lambda = 0.85\ \mu m$ still apears but slightly blueshifts. For a free-standing active layer, the normal absorptance is less than 0.15 particularly in the wavelength range from $\lambda = 0.7\ \mu m$ to the bandgap due to the small intrinsic absorption coefficient of GaSb material [91].

IV.5.1.1.1 Excitation of Magnetic Polariton (MP) resonance

The resonance peak at $\lambda = 1.69\ \mu m$ is attributed to the excitation of magnetic polariton (MP). To explain the underlying mechanism for the absorption peak, the electromagnetic power density at the *x*-*z* cross-section inside the structure is illustrated in Fig. 4.5 (a). The nanostructured Ag grating, the GaSb layer, and the Ag back reflector in two periods are illustrated. It can be seen that the electric field inside the GaSb active layer forms a current loop between the upper Ag grating and the lower Ag substrate. In addition, the magnetic field is confined in the GaSb layer with one order of magnitude higher than the incident one, indicating strong light confinement at the resonance wavelength $\lambda = 1.69 \mu m$. These features are the main characteristics of MP resonance, which have been deeply discussed in Refs [95], [96], [97].

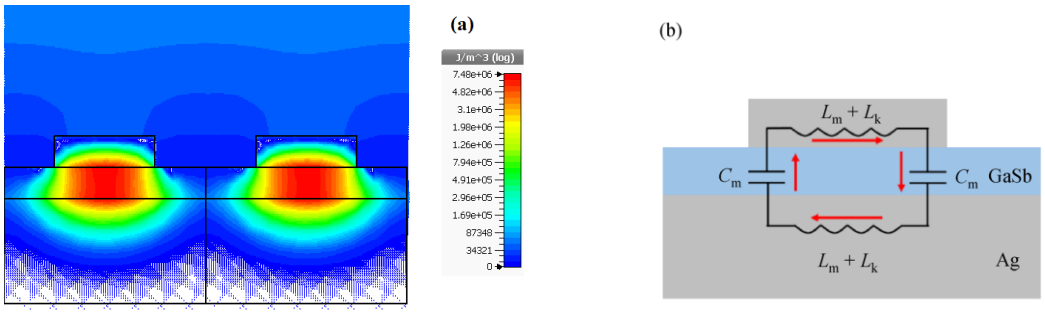

Fig.4. 5: (a) Electromagnetic power density at $\lambda = 1.69$ µm for normal incidence where MP is excited under TM waves; **(b)** schematic of the LC circuit model described by *Qing et al* [91]

The GaSb layer between the top grating ridge and the Ag back reflector can be considered as a capacitor with capacitance C_m, while the top nanostructured Ag grating and the bottom Ag back reflector can be treated as inductors with inductances L_m and L_k respectively represent the parallel-plate inductance and the kinetic one. The expressions for C_m, L_m and L_k are listed below [98].

$$C_m = \frac{c_1 \varepsilon_0 \varepsilon_d w}{d} \qquad \textbf{Eq (4. 16)}$$

$$L_m = 0.5 \mu_0 w d \qquad \textbf{Eq (4. 17)}$$

$$L_k = \frac{-w}{\omega^2 \varepsilon_0 \varepsilon_m^{'} \delta^{'}} \qquad \textbf{Eq(4. 18)}$$

where c_1 is a coefficient accounting for non-uniform charge distribution at the metal surface and it is in the range $0.2 \le c_1 \le 0.3$ [99], ε_0 is the permittivity of vacuum, ε_d is the permittivity of the GaSb layer, μ_0 is the permeability of vacuum, and $\varepsilon_m^{'}$ is the real part of the permittivity of Ag. $\delta = \lambda / 4\pi k$ is the skin depth of Ag material[100], where λ is the wavelength of the incident wave, and *k* is the extinction coefficient of Ag. The total impedance of the LC circuit model is[100]:

$$Z_{total} = 2\omega(L_m + L_k) - \frac{2}{\omega C_m} \qquad \textbf{Eq (4. 19)}$$

Magnetic resonance occurs when the total impedance of the circuit is zero, i.e., $Z_{total} = 0$, which yields the analytical MP resonance wavelength:

$$\lambda_{MP} = 2\pi c_0 \sqrt{C_m (L_m + L_K)} \qquad \textbf{Eq (4. 20)}$$

The empirical model can give a simple explanation of some absorption peaks, but FDTD and FEM give a profound study of different optical phenomena, with the opportunity to compute electromagnetic fields scattered and/or absorbed by each layer in the design.

IV.5.1.1.2Excitation of SPP modes

The absorption peak at λ = 0.85 μm for the ultrathin TPV cell-coupled MTM structure under normal incident TM waves is due to the excitation of SPP modes at the air-nanostructured Ag grating interface. SPP waves represent the interaction between electromagnetic waves and the oscillatory movement of free charges near the surface of the metal materials [101]. The excitation of SPP between two nonmagnetic materials is determined by the dispersion relation at TM polarization [98]:

$$k_{spp} = (\omega / c_0)\sqrt{\varepsilon_1 \varepsilon_2 / (\varepsilon_1 + \varepsilon_2)} \qquad \textbf{Eq (4. 21)}$$

where k_{SPP} denotes the wavevector of the SPP mode, ε_1 and ε_2 are the dielectric functions of the materials at each side of the interface respectively, whose real parts should have opposite signs to excite SPP, ω is the angular frequency and c_0 is the speed of light in air. The SPP dispersion curve for a planar interface usually lies on the right side of the light line due to the nature of evanescent waves. However, SPP can be excited with propagation waves with periodic gratings because large in-plane wavevectors can be matched by high-order diffracted waves according to the Bloch-Floquet condition [101]:

$$k_{x,j} = k_x + \frac{2\pi j}{\Lambda} \qquad \textbf{Eq(4. 22)}$$

where *j* is the diffraction order in the *x*-direction and $k_x = \omega / c$ is the parallel component of the wavevector in a vacuum. The resonance frequency for SPP modes can be theoretically obtained by solving $\left|k_{SPP}\right| = \left|k_{x.j}\right|$. The wavelength at which SPP is excited at the air-Ag interface is predicted to be $\lambda_{SPP} = 0.85\mu m$, which matches well with a peak at ($\lambda = 0.87\mu m$) from our simulation.

IV.5.1.1.3 Excitation of Fabry-Perot (FP) resonance

When the ultrathin GaSb layer was located on an Ag back reflector to form a GaSb-Ag configuration, it is observed that there is an absorption peak at ($\lambda = 0.35\mu m$) with an absorptance α= 0.85, as shown in Fig. 4.4. This peak is attributed to interference inside the GaSb layer. The spectral normal reflectance $\left(R_\lambda\right)$ of the GaSb-Ag structure can also be analytically calculated by the thin-film optics method [101]:

$$R_\lambda = \left| \frac{r_{12} + r_{23} e^{2i\beta}}{1 + r_{12} r_{23} e^{2i\beta}} \right|^2 \qquad \textbf{Eq (4. 23)}$$

where r_{12} is the reflection coefficient at the interface from air to GaSb and r_{23} is the reflection coefficient at the interface from GaSb to Ag. $\beta = 2\pi n_2 d \cos\theta_2 / \lambda$ is the phase shift inside the ultrathin GaSb layer, where n_2 is the refractive index of GaSb and θ_2 is the refraction angle inside GaSb. The absorptance of the GaSb-Ag structure can be calculated by $A_\lambda = 1 - R_\lambda$ due to its opaqueness. To verify that the absorption peak $\lambda = 0.87\mu m$ is caused by the excitation of FP resonance, the total phase shift ψ in the ultrathin active GaSb layer is calculated by [101]

$$\psi = \phi_1 + \phi_2 + 2\beta \qquad \textbf{Eq(4. 24)}$$

where $\phi_1 = \arg(r_{21})$ and $\phi_2 = \arg(r_{23})$ are the phase shifts caused by the reflection at the interface from GaSb to air and the interface from GaSb to Ag, respectively. FP resonance occurs when the total phase shift in the active layer is a multiple of *2π*, leading to standing waves existing in the cavity. The calculated phase shift ψ at $\lambda = 0.87\mu m$ is zero, which means that there exists a constructive interference effect inside the thin-film GaSb layer thus improving the light trapping mechanism. When an Ag grating is added onto the GaSb-on-Ag configuration to form an ultrathin TPV cell-coupled metamaterial structure, the upper Ag grating layer modifies the reflection coefficient r_{12} at the top interface of GaSb which becomes an air-Ag-GaSb interface, resulting in a slight peak shift from $\lambda = 0.84\mu m$ to $0.87\ \mu m$ under TM waves as shown in Fig. 4.4 . Therefore, it is reasonable to deduce that this absorption peak at $\lambda = 0.87\mu m$ in the ultrathin TPV cell-coupled MTM structure is also caused by FP resonance [102]. Note that, FP resonance also results in a similar absorption peak for TE waves but at a slightly different wavelength $\lambda = 0.74\mu m$, as shown in Figure. 4.4.

IV.5.1.2 Geometric dependence of MP, SPP, and FP resonances

The effects of geometric parameters on the MP, SPP, as well as FP have been evaluated. The normal absorptance of the ultrathin TPV cell-coupled MTM structure was calculated by independently varying grating width (*w*), period (*A*), and active layer thickness (*d*), and maintaining the values of the rest geometric parameters. Figure.4.6 (a) shows the spectral absorbance of the structure with grating width changing from 80 *nm* to 120 *nm*. It can be observed that the absorption peak due to the excitation of MP shifts to longer wavelengths when the grating width increases, which is consistent with previous results [103]. Figure.4.6 (b) shows the comparison of the MP resonance peak simulation as a function of grating width, MP resonance

wavelength monotonically increases with the grating width (*w*), which is due to the increase of the capacitance and inductance values according to Equations. (4.16;4.18) as well as a monotonically decreasing absorbance rate. On the other hand, the absorption peak associated with SPP and the one associated with FP is little affected by the grating width, as SPP peaks only depend on the grating period according to the dispersion relation, and FP peaks only depend on the spacer thickness according to a marked phase shift.

Figure.4.6 (c), (d) shows the spectral absorptance with the grating period (*A*) changing from 150 to 250 *nm*. Here the SPP peak barely changes with the grating period, which is different from the previous results [98]**,** where the SPP resonance wavelength increases with the grating period. Therefore, the influence of the cell period on the SPP resonance wavelength is negligible. On the other hand, the grating period does not affect the FP peak wavelength but slightly shifts the MP peak location as can be observed in Figure. 4.6(c), (d).

Figure .4.6(e) and (f) show the spectral absorptance with the spacer thickness changing from 20 *nm* to 50 *nm*. It can be seen that the FP peak shifts to longer wavelengths when the spacer thickness increases in TE mode, agreeing well with the result predicted by the phase shift in Eq. (4.17), as shown in Figure.4.6 (f). This is due to the increase of the phase shift in the ultrathin active layer. On the other hand, the SPP peak is not affected by the spacer thickness and the MP absorbance peak strongly changes when *d* is larger than 30 *nm*.

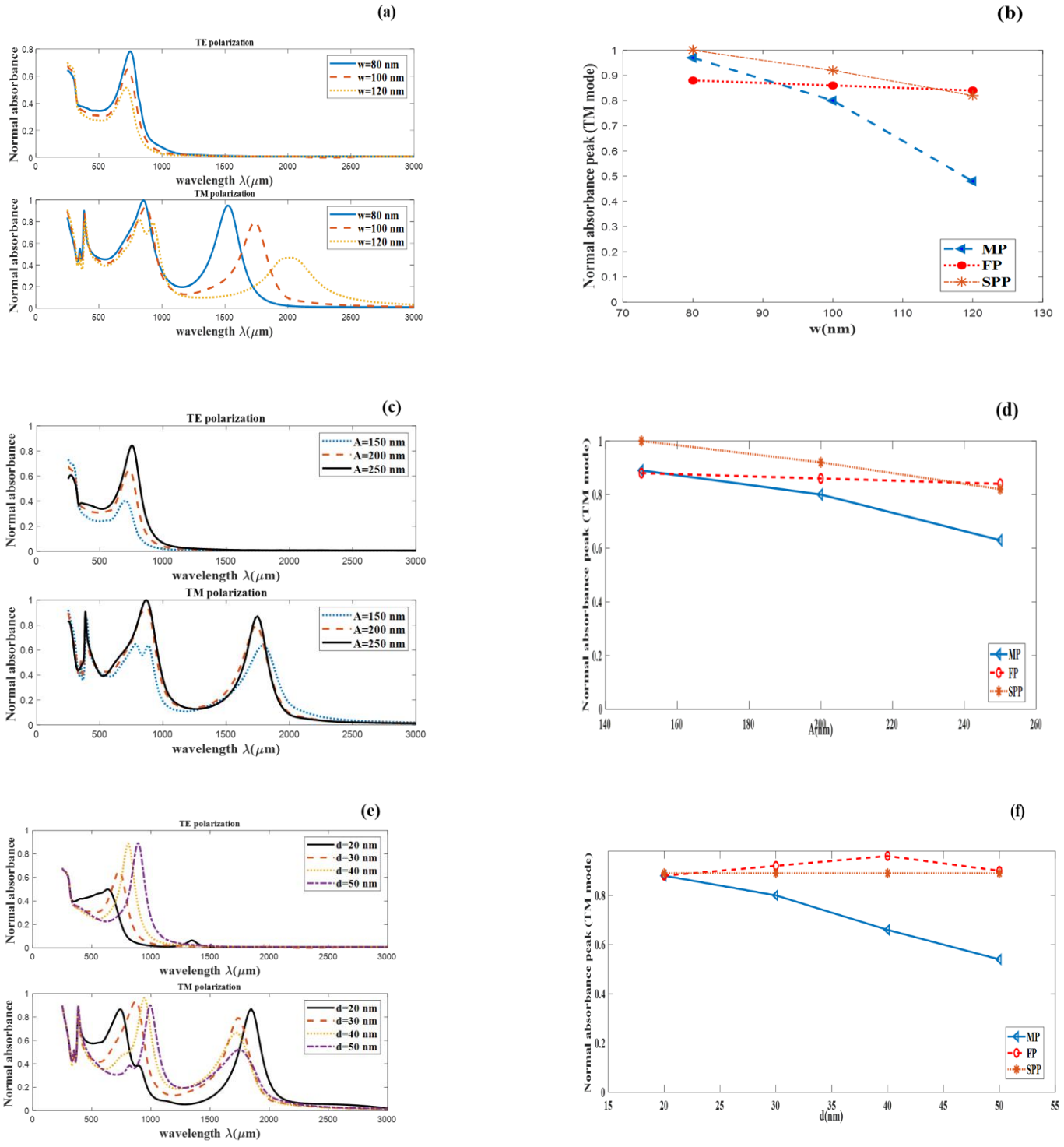

Fig.4. 6: (a) The normal absorptance with varying grating width (*w*); **(b)** Comparison of the MP, FP, and SPP resonances with varying grating width; **(c)** The normal absorptance spectra with the varying grating period (A); **(d)** Comparison of the MP, FP, and SPP resonances with the varying grating period (A); **(e)** The spectral normal absorptance with varying spacer thickness (d); **(f)** Comparison of the MP, FP, and SPP resonances with varying spacer thickness (*d)*.

IV.5.1.3 Behaviors of MP, SPP, and FP at oblique incidences

Figure. 4.7 illustrates the contours of the spectral-directional absorptance of an ultrathin TPV cell-coupled MTM structure in terms of wavelength and incident angle for TM and TE polarization to gain insight into the behavior of MP, SPP, and FP at oblique incidences. As shown in Figure.4.7(b), there are three bright bands under TM waves, which indicate three major absorption peaks. The first one around $\lambda = 1.6\mu m$ is attributed to the excitation of MP. The flatness of the band indicates that the excitation wavelength of MP does not change at oblique incidence angles, which is consistent with the observations from previous studies [98]. The second one around $\lambda = 0.2\mu m$ is associated with FP resonance for TM modes. It can be seen that we have two regions for the FP resonance under TE polarization, which barely decrease under the highest incidence angles. The third one around $\lambda = 0.8\mu m$ is because of the principal excitation of SPP. Note that the principal SPP resonance condition is too insensitive to the incidence angle work, but exhibits new SPPs modes for large incident angles, which is due to the small nanostructured Ag grating period. On the other hand, as shown in Figure. 4.7(a), under TE waves there is only the bright band due to FP resonance, as MP and SPP can only be excited under TM waves for 1D grating structures. Note that the FP resonance is insensitive to the incidence angle [91]. Moreover, the absorption due to FP resonance under TE waves is much weaker than that under-TM waves.

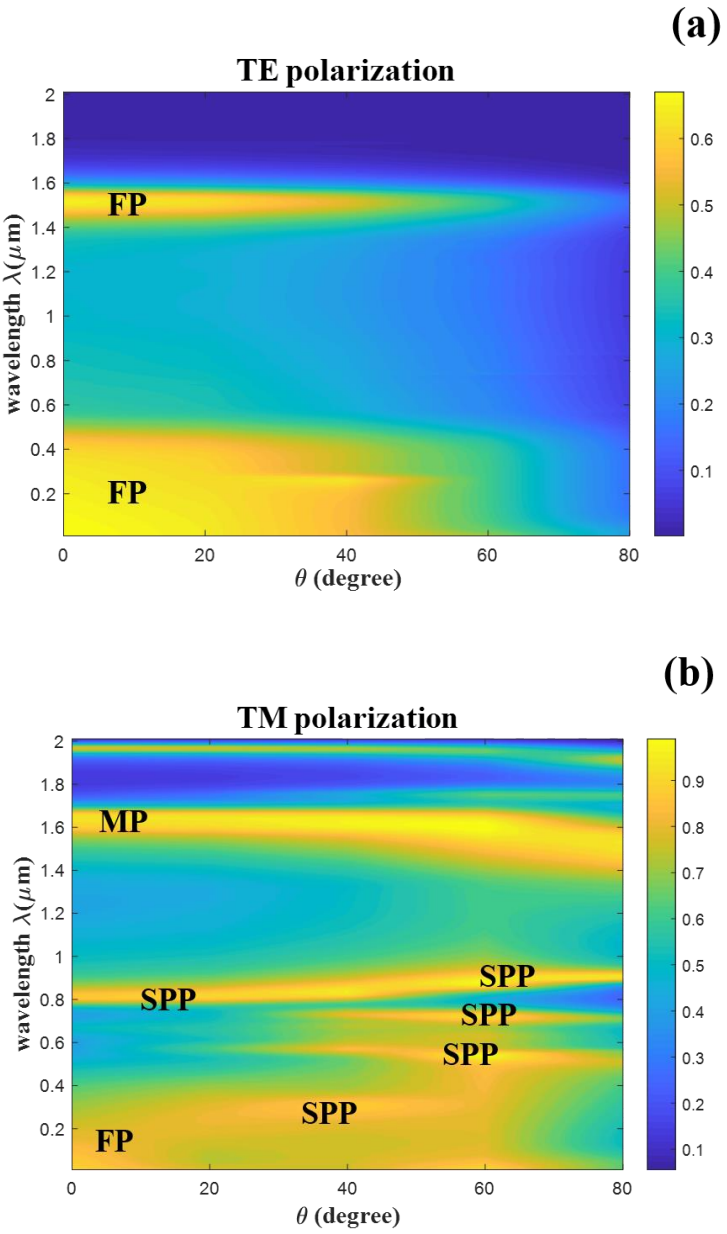

Fig.4. 7: Contour of the spectral-directional absorptance of the ultrathin TPV cell-coupled Metamaterial structure as a function of wavelength and angle of incidence **(a)** TE modes, and **(b)** TM modes.

IV.5.1.4 Energy absorbed by the ultrathin GaSb layer

Although light absorption can be significantly improved in the ultrathin TPV cell-coupled Metamaterial structure by exciting MP, SPP, and FP resonances, only the energy absorbed by the active layer can contribute to the photon-generated carriers, while the energy absorbed by metals in the structure is lost. Therefore, it is important to evaluate the amount of energy absorbed by the active layer rather than that by the entire structure. The entire structure can be divided into three layers: the first layer is the Ag grating, the second one is the GaSb layer, and the third one is the Ag substrate. The energy absorbed per unit volume inside each layer can be obtained by [104]:

$$P_i = \frac{1}{2}\varepsilon_0 \varepsilon_i^{"} \omega \left|E_i\right|^2 \qquad \textbf{Eq (4. 25)}$$

and the absorbed power in each layer can be normalized to the incident power [104]:

$$Abs_i = \frac{\int P_i dV_i}{0.5 c_0 \varepsilon_0 \varepsilon_i^{"} \omega \left|E_{inc}\right|^2 A_r} \qquad \textbf{Eq (4. 26)}$$

where $\varepsilon_i^{"}$ is the imaginary part of the relative permittivity of layer *i*, V_i is the volume of layer *i*, A_i is the area that the light source is incident upon, E_i is the electric field inside layer *i*, and E_{inc} is the incident electric field.

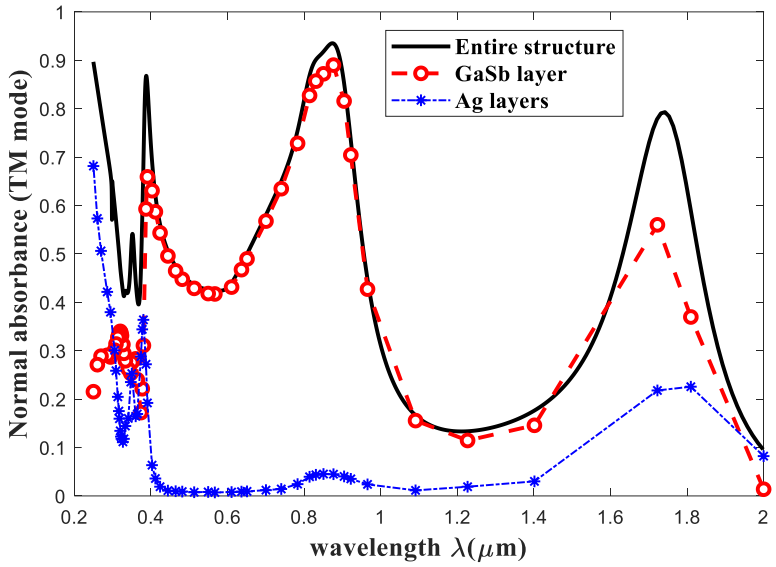

Fig.4. 8: The spectral absorbance of the ultrathin TPV cell-coupled metamaterial structure

The power absorbed by the entire structure is simply the sum of the energy absorbed by each layer. Figure 4.8 shows the normalized energy absorption in the GaSb layer, the metals, and the entire structure. It can be seen that most of the energy is absorbed by the GaSb active layer, while some non-negligible energy between 1.5 μm to 2 μm is absorbed by Ag layers.

IV.5.1.5 Electrical properties and TPV performance of the ultrathin GaSb cell

To evaluate the performance of the ultrathin TPV cell-coupled metamaterial structure as an ultrathin TPV cell, short-circuit current density, open-circuit voltage, output electric power, and cell efficiency were calculated. The short-circuit current density $J_{sc}(A/cm^2)$ is calculated by [105]

$$J_{sc} = \int_0^{\frac{hc_0}{E_g}} \frac{e\lambda}{hc_0} a(\lambda)\eta_i(\lambda)q(\lambda)d\lambda \qquad \textbf{Eq (4. 27)}$$

where *h* is Planck's constant, E_g is the bandgap of the GaSb cell (0.72 eV), $\alpha(\lambda)$ is the normalized energy absorption in the GaSb layer only (average value over TM and TE waves), *e* is an elementary charge, $\eta_i(\lambda)$ is the External quantum efficiency (EQE) of the GaSb cell, and $q(\lambda)$ is the radiative heat flux from a TPV emitter. The EQE of the ultrathin GaSb cell in this calculation is assumed to be 100% according to *Qing* et al[106], as a perfect EQE of TPV cell, in our calculation we took the true values of EQE of the ultrathin from Ref [106]. Because the large recombination losses for minority carriers are significantly reduced and the surface recombination losses can also be significantly reduced using a good passivation layer. The radiative heat flux from a blackbody emitter can be calculated by [107]:

$$E_{b\lambda}(T) = \frac{C_1}{\lambda^5\left[\exp(C_2/\lambda T)-1\right]} \qquad \textbf{Eq (4. 28)}$$

where $C_1 = 3.742\times10^8 W.\mu m^4/m^2$, $C_2 = 1.439\times10^4\,\mu m.K$, and *T* is the blackbody temperature. The total incident radiative flux onto the TPV cell P_{in} can be calculated by [107]:

$$P_{in} = \int_0^\infty E_{b\lambda}(T)\varepsilon_\lambda d\lambda \qquad \textbf{Eq(4. 29)}$$

where ε_λ is the spectral emissivity of a diffuse TPV intermediate emitter which is supposed perfect in our study. The open-circuit voltage V_{oc} is calculated by [105]:

$$V_{oc} = \left(k_B T_c / e\right)\ln\left(J_{sc}/J_0 + 1\right) \qquad \textbf{Eq (4. 30)}$$

where k_B is the Boltzmann constant, T_c is the cell temperature which is assumed to be 300 K, and J_0 is the dark current which can be calculated by [105]

$$J_0 = e\left(\frac{n_i^2 D_h}{L_h N_D} + \frac{n_i^2 D_e}{L_e N_A}\right) \quad \textbf{Eq (4. 31)}$$

where n_i is the intrinsic carrier concentration of GaSb, N_D and N_A are respectively the donor concentration and acceptor concentration, D_h and D_e are respectively the hole diffusion coefficient and electron diffusion coefficient, and L_h and L_e are respectively the hole and electron diffusion length. The parameters for calculating J_0 are from Ref [108]. The output electric power P_{cell} can be calculated by [105]

$$P_{cell} = J_{sc} V_{oc} \left(1 - 1/y\right)\left[1 - \ln\left(y\right)/y\right] \quad \textbf{Eq(4. 32)}$$

where $y = 1n(J_{sc} / J_0)$. Finally, the heat-to-electricity conversion efficiency for this ultrathin TPV cell-coupled Metamaterial cell can be expressed as the ratio of the output electric power P_{cell} to the total incident radiative heat flux P_{in} [91]:

$$\eta = \frac{P_{cell}}{P_{in}} \quad \textbf{Eq (4. 33)}$$

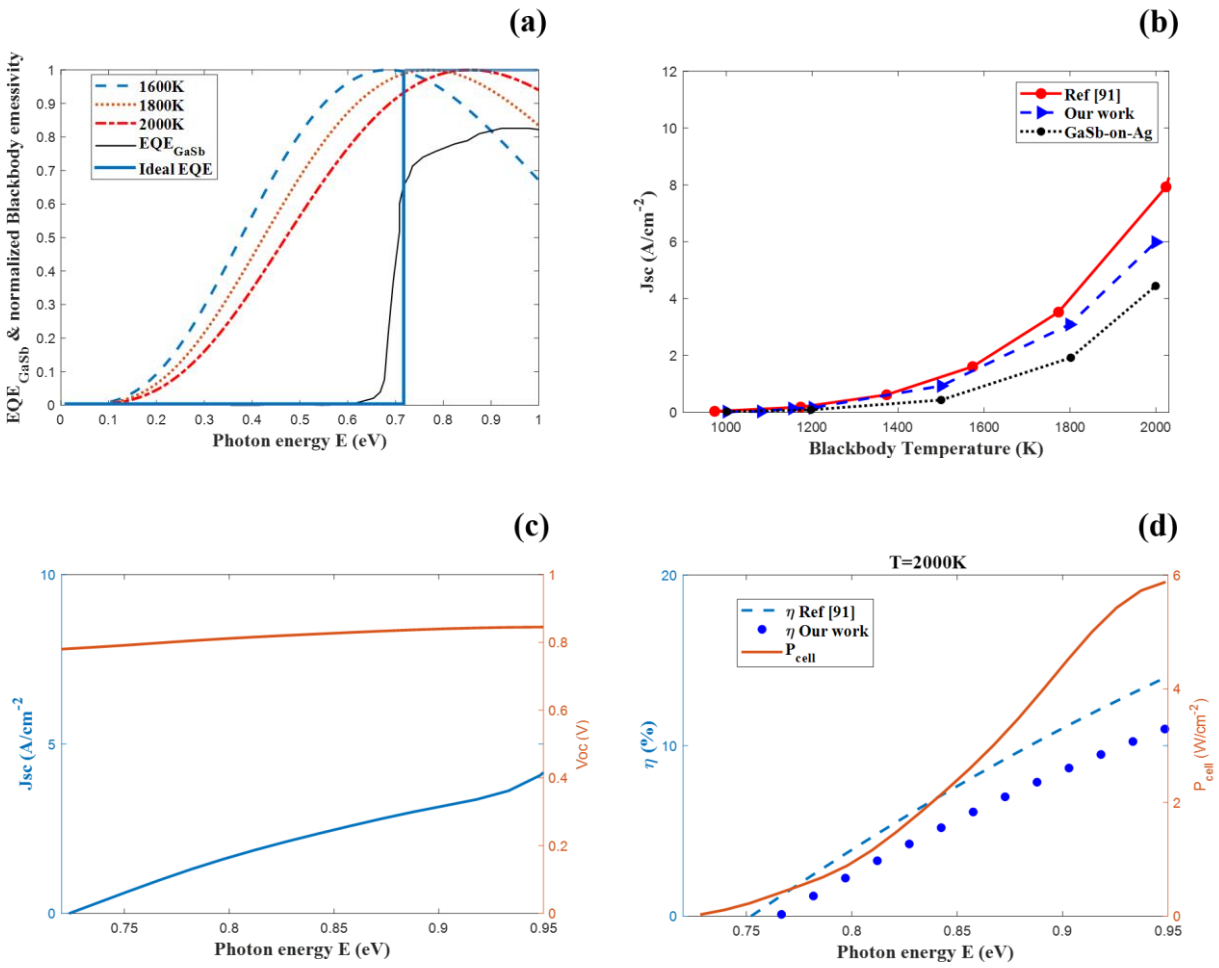

Fig.4. 9*:* **(a)** Normalized Spectral for radiative heat fluxes from a blackbody at different temperatures. The EQE for the ideal case of Ref [91], and the true case of the active layer [106], are also presented; **(b)** the short circuit current J_{sc} in TPV cell under blackbody radiation with different blackbody temperatures; **(c)** the effect of the incoming wavelength on J_{sc} and V_{oc}; **(d)** P_{cell}, and η variation under blackbody radiation of T = 2000 K.

Figure 4. 9(a) shows the spectral distribution of radiative heat fluxes from blackbody sources at temperatures from 1600 to 2000 K, with EQE of the GaSb active layer. As we can see here the adequate Blackbody for the cell is 2000 K. Thus enhancing the TPV efficiency is required a good choice of Blackbody temperature [1].

Figure 4.9(b) shows the short-circuit current of the ultrathin GaSb cell under blackbody radiation at different temperatures. a good agreement with Quing et al results has been observed here, the

variation between them induced by using a true EQE for the active layer. The short-circuit current can be greatly enhanced with the ultrathin TPV cell-coupled Metamaterial structure and increases with the blackbody temperature. For example, when the blackbody temperature is 2000 K, the short-circuit current of the ultrathin GaSb cell with an ultrathin TPV cell-coupled metamaterial structure is $5.95 A/cm^2$, which is two times the short-circuit current of a free-standing GaSb active layer.

Figures 4. 9(c) and (d) show the effect of incoming wavelength on the GaSb cell under blackbody radiation of 2000 K. Here the varying wavelength range impacts directly the performance of the GaSb TPV cell. The wavelength has a significant influence on the cell performance. As the wavelength increases the short-circuit current J_{sc} increases, while open-circuit voltage V_{oc} barely changes. The output electric power P_{cell} also decreases when decreasing the P_{in} (incoming wavelength) decreases at a faster rate, resulting in increasing cell efficiency η . The maximum cell efficiency can be obtained $\eta_{\max} = 11.3\%$, which is related to the MP, SPP, and FP peaks contributing to the cell conversion efficiency.

IV.5.1.6 Conclusion

In this chapter a Plasmonic light-trapping structure has been simulated, using several numerical approaches such as FDTD, TLM, and FEM. The CST MICROWAVE STUDIO optical software has been managed to analyze and simulate the nanostructured structure under different modes of polarization and for a wide wavelength range from infrared to visible. We have numerically verified that the absorption of visible and near-infrared light in an ultrathin GaSb layer can be greatly enhanced with an MTM structure through the plasmonic phenomenon. The mechanism for the absorption enhancement near the bandgap of the active layer is shown to be the excitation of MP, which has been clarified with the electromagnetic power distribution. Moreover, SPP and FP resonance are excited at visible wavelengths for selective absorption. It is seen that the MP resonance wavelength can be easily tuned by changing the grating width, and the FP resonance wavelength can be adjusted by changing the spacer thickness. With the coupled plasmonic structure, the short-circuit current in the ultrathin GaSb cell is greatly enhanced. The cell conversion efficiency can be further improved up to 11.3% under blackbody radiation of 2000K. The results and understanding gained here will facilitate the evelopment of next-generation low-cost high-efficiency ultrathin infrared thermophotovoltaic and hybrid cells.

Overall conclusion

The work contained in this manuscript started by studying and modeling a variety of TPV technologies. The key components of an efficient TPV system are light management and the high-quality choice of TPV cells. Our choice of Plasmonic-based light trapping of ultrathin TPV cells operating at visible and near-infrared wavelengths is based on a new design suggested by the USA research team (Qing et al 2018), first of all, the optical simulation of the structure is numerically modeled by the FEM and FDTD method by (CST MICROWAVE STUDIO). The under-study design with an ultrathin GaSb active layer scores a remarkable TPV conversion efficiency of up to 11.3% under blackbody radiation of 2000K, this is a good conversion efficiency compared to its thin dimension. In conclusion, it is evident that this study has shown that the suggested ultrathin TPV cell and by using a Metamaterials-based light trapping management system can operate efficiently at a high temperature, and revealed that they may operate at high and modest (wasted heat) temperatures all at one system if we optimize the suggested design. These findings will assist to grow up in the next-generation ultrathin PV and TPV cells and detectors that are inexpensive and efficient. Our future work will be focused on the combination of two or three ultrathin active layers cells into a single tandem cell structure based on plasmonic light trapping enhancement between them to convert as possible the incident waves for the largest working temperature range.

Bibliography

[1] T. Bauer, *Thermophotovoltaics: Basic Principles and Critical Aspects of System Design*. Berlin Heidelberg: Springer-Verlag Berlin and Heidelberg GmbH & Co. K, 2011.

[2] C. Ferrari, F. Melino, M. Pinelli, P. R. Spina, and M. Venturini, "Overview and Status of Thermophotovoltaic Systems," *Energy Procedia*, vol. 45, pp. 160–169, Jan. 2014, doi: 10.1016/j.egypro.2014.01.018.

[3] G. Colangelo, A. de Risi, and D. Laforgia, "New approaches to the design of the combustion system for thermophotovoltaic applications," *Semicond. Sci. Technol.*, vol. 18, no. 5, p. S262, Apr. 2003, doi: 10.1088/0268-1242/18/5/318.

[4] G. Mattarolo, *Development and Modelling of a Thermophotovoltaic System*. kassel university press GmbH, 2007.

[5] F. Bendelala, "Modeling and performances optimization of thermophotovoltaic cells based on new metamaterials."

[6] T. J. Coutts, "A review of progress in thermophotovoltaic generation of electricity," *Renew. Sustain. Energy Rev.*, vol. 3, no. 2–3, pp. 77–184, 1999.

[7] M. Herrando and C. N. Markides, "Hybrid PV and solar-thermal systems for domestic heat and power provision in the UK: Techno-economic considerations," *Appl. Energy*, vol. 161, pp. 512–532, Jan. 2016, doi: 10.1016/j.apenergy.2015.09.025.

[8] D. Wilt, D. Chubb, D. Wolford, P. Magari, and C. Crowley, "Thermophotovoltaics for Space Power Applications," *AIP Conf. Proc.*, vol. 890, pp. 335–345, Feb. 2007, doi: 10.1063/1.2711751.

[9] L. Broman and J. Marks, "Co-generation of electricity and heat from combustion of wood powder utilizing thermophotovoltaic conversion," *AIP Conf. Proc.*, vol. 321, no. 1, pp. 133–138, Jan. 1995, doi: 10.1063/1.47062.

[10] A. S. Vlasov, V. P. Khvostikov, O. A. Khvostikova, P. Y. Gazaryan, S. V. Sorokina, and V. M. Andreev, "TPV Systems with Solar Powered Tungsten Emitters," *AIP Conf. Proc.*, vol. 890, no. 1, pp. 327–334, Feb. 2007, doi: 10.1063/1.2711750.

[11] P. A. Jurczak, "Development of III-V Semiconductor Materials for Thermophotovoltaic Cells," Doctoral, UCL (University College London), 2017. Accessed: Mar. 30, 2023. [Online]. Available: https://discovery.ucl.ac.uk/id/eprint/10026102/

[12] G. Beghi, *Performance of Solar Energy Converters: Thermal Collectors and Photovoltaic Cells: Lectures of a Course held at the Joint Research Centre, Ispra, Italy, November 11–18, 1981*. Springer Science & Business Media, 2012.

[13] P. M. Fourspring *et al.*, "Thermophotovoltaic Spectral Control," *AIP Conf. Proc.*, vol. 738, no. 1, pp. 171–179, Nov. 2004, doi: 10.1063/1.1841892.

[14] F. Bendelala, "Modeling and performances optimization of thermophotovoltaic cells based on new metamaterials."

[15] B. Bitnar, W. Durisch, and A. Waser, "TPV Systems — From Research Towards Commercialisation," *AIP Conf. Proc.*, vol. 738, no. 1, pp. 33–41, Nov. 2004, doi: 10.1063/1.1841877.

[16] W. E. Horne, M. D. Morgan, V. S. Sundaram, and T. Butcher, "500 Watt Diesel Fueled TPV Portable Power Supply," *AIP Conf. Proc.*, vol. 653, no. 1, pp. 91–100, Jan. 2003, doi: 10.1063/1.1539367.

[17] W. R. Chan, V. Stelmakh, C. M. Waits, M. Soljacic, J. D. Joannopoulos, and I. Celanovic, "Photonic Crystal Enabled Thermophotovoltaics for a Portable Microgenerator," *J. Phys. Conf. Ser.*, vol. 660, no. 1, p. 012069, Nov. 2015, doi: 10.1088/1742-6596/660/1/012069.
[18] H. Sai, T. Kamikawa, Y. Kanamori, K. Hane, H. Yugami, and M. Yamaguchi, "Thermophotovoltaic Generation with Microstructured Tungsten Selective Emitters," *AIP Conf. Proc.*, vol. 738, no. 1, pp. 206–214, Nov. 2004, doi: 10.1063/1.1841896.
[19] M. G. Mauk, O. V. Sulima, J. A. Cox, and R. L. Mueller, "Low-bandgap (0.3 to 0.5 eV) InAsSbP thermophotovoltaics: assessment for open-circuit voltage improvements," in *Proceedings of 3rd World Conference onPhotovoltaic Energy Conversion, 2003*, May 2003, pp. 224-227 Vol.1.
[20] L. Besra and M. Liu, "A review on fundamentals and applications of electrophoretic deposition (EPD)," *Prog. Mater. Sci.*, vol. 52, no. 1, pp. 1–61, Jan. 2007, doi: 10.1016/j.pmatsci.2006.07.001.
[21] D. Chubb, *Fundamentals of Thermophotovoltaic Energy Conversion*. Elsevier, 2007.
[22] J. Kilner, S. Skinner, S. Irvine, and P. Edwards, *Functional materials for sustainable energy applications*. Elsevier, 2012. Accessed: Mar. 30, 2023. [Online]. Available: https://ora.ox.ac.uk/objects/uuid:1396caf0-af99-489f-9757-f8bdb860cedc
[23] Z. Utlu and B. S. Önal, "Thermodynamic analysis of thermophotovoltaic systems used in waste heat recovery systems: an application," *Int. J. Low-Carbon Technol.*, vol. 13, no. 1, pp. 52–60, Mar. 2018, doi: 10.1093/ijlct/ctx019.
[24] D. M. Wilt, R. J. Wehrer, W. F. Maurer, P. P. Jenkins, B. Wernsman, and R. W. Schultz, "Buffer Layer Effects on Tandem InGaAs TPV Devices," *AIP Conf. Proc.*, vol. 738, no. 1, pp. 453–461, Nov. 2004, doi: 10.1063/1.1841924.
[25] L. B. Karlina, A. S. Vlasov, M. M. Kulagina, and N. Kh. Timoshina, "Thermophotovoltaic cells based on In0.53Ga0.47As/InP heterostructures," *Semiconductors*, vol. 40, no. 3, pp. 346–350, Mar. 2006, doi: 10.1134/S1063782606030171.
[26] V. S. Sundaram *et al.*, "GaSb based ternary and quaternary diffused junction devices for TPV applications," in *Third NREL Conference on thermophotovoltaic generation of electricity*, Colorado Springs, Colorado (USA): ASCE, 1997, pp. 105–115. doi: 10.1063/1.53277.
[27] O. V. Sulima, R. Beckert, A. W. Bett, J. A. Cox, and M. G. Mauk, "InGaAsSb photovoltaic cells with enhanced open-circuit voltage," *IEE Proc. - Optoelectron.*, vol. 147, no. 3, pp. 199–204, Jun. 2000, doi: 10.1049/ip-opt:20000500.
[28] A. W. Bett and O. V. Sulima, "GaSb photovoltaic cells for applications in TPV generators," *Semicond. Sci. Technol.*, vol. 18, no. 5, pp. S184–S190, May 2003, doi: 10.1088/0268-1242/18/5/307.
[29] M. G. Mauk, O. Sulima, J. A. Cox, and R. L. Mueller, "Low-bandgap (0.3 to 0.5 eV) InAsSbP thermophotovoltaics: Assessment for open-circuit voltage improvements," Jun. 2003, pp. 224-227 Vol.1. doi: 10.1109/WCPEC.2003.1305262.
[30] V. M. Andreev, "Low-Bandgap Ge and InAsSbP/InAs-Based TPV Cells," in *AIP Conference Proceedings*, Rome (Italy): AIP, 2003, pp. 383–391. doi: 10.1063/1.1539393.
[31] P. S. Dutta, "GaSb and Ga1−xInxSb Thermophotovoltaic Cells using Diffused Junction Technology in Bulk Substrates," in *AIP Conference Proceedings*, Rome (Italy): AIP, 2003, pp. 392–401. doi: 10.1063/1.1539394.
[32] D. M. Wilt, "Buffer Layer Effects on Tandem InGaAs TPV Devices," in *AIP Conference Proceedings*, Freiburg (Germany): AIP, 2004, pp. 453–461. doi: 10.1063/1.1841924.

[33] V. Khvostikov *et al.*, “Thermophotovoltaic Cells Based on Low-Bandgap Compounds,” vol. 738, Nov. 2004, doi: 10.1063/1.1841922.
[34] L. B. Karlina, A. S. Vlasov, M. M. Kulagina, and N. Kh. Timoshina, “Thermophotovoltaic cells based on In0.53Ga0.47As/InP heterostructures,” *Semiconductors*, vol. 40, no. 3, pp. 346–350, Mar. 2006, doi: 10.1134/S1063782606030171.
[35] M. W. Dashiell *et al.*, “Quaternary InGaAsSb Thermophotovoltaic Diodes,” *IEEE Trans. Electron Devices*, vol. 53, no. 12, pp. 2879–2891, Dec. 2006, doi: 10.1109/TED.2006.885087.
[36] M. K. Hudait, M. Brenner, and S. A. Ringel, “Metamorphic In0.7Al0.3As/In0.69Ga0.31As thermophotovoltaic devices grown on graded InAsyP1−y buffers by molecular beam epitaxy,” *Solid-State Electron.*, vol. 53, no. 1, pp. 102–106, Jan. 2009, doi: 10.1016/j.sse.2008.10.007.
[37] K. J. Cheetham, P. J. Carrington, N. B. Cook, and A. Krier, “Low bandgap GaInAsSbP pentanary thermophotovoltaic diodes,” *Sol. Energy Mater. Sol. Cells*, vol. 95, no. 2, pp. 534–537, Feb. 2011, doi: 10.1016/j.solmat.2010.08.036.
[38] R. S. Tuley, J. M. S. Orr, R. J. Nicholas, D. C. Rogers, P. J. Cannard, and S. Dosanjh, “Lattice-matched InGaAs on InP thermophovoltaic cells,” *Semicond. Sci. Technol.*, vol. 28, no. 1, p. 015013, Jan. 2013, doi: 10.1088/0268-1242/28/1/015013.
[39] Y.-Y. Lou, X.-L. Zhang, A.-B. Huang, and Y. Wang, “Enhanced thermal radiation conversion in a GaSb/GaInAsSb tandem thermophotovoltaic cell,” *Sol. Energy Mater. Sol. Cells*, vol. 172, pp. 124–132, Dec. 2017, doi: 10.1016/j.solmat.2017.07.030.
[40] Q. Lu, R. Beanland, D. Montesdeoca, P. J. Carrington, A. Marshall, and A. Krier, “Low bandgap GaInAsSb thermophotovoltaic cells on GaAs substrate with advanced metamorphic buffer layer,” *Sol. Energy Mater. Sol. Cells*, vol. 191, pp. 406–412, Mar. 2019, doi: 10.1016/j.solmat.2018.11.036.
[41] M. M. A. Gamel *et al.*, “A Review on Thermophotovoltaic Cell and Its Applications in Energy Conversion: Issues and Recommendations,” *Materials*, vol. 14, no. 17, p. 4944, Aug. 2021, doi: 10.3390/ma14174944.
[42] J. Chunder Bose, “On the Rotation of Plane of Polarisation of Electric Waves by a Twisted Structure,” *Proc. R. Soc. Lond. Ser. I*, vol. 63, pp. 146–152, Jan. 1898.
[43] M. Benattalah, “Design study of high-efficiency thermophotovoltaic solar cell.,” 2020.
[44] D. R. Smith, W. J. Padilla, D. C. Vier, S. C. Nemat-Nasser, and S. Schultz, “Composite Medium with Simultaneously Negative Permeability and Permittivity,” *Phys. Rev. Lett.*, vol. 84, no. 18, pp. 4184–4187, May 2000, doi: 10.1103/PhysRevLett.84.4184.
[45] C. G. Christodoulou and P. Wahid, *Fundamentals of Antennas: Concepts and Applications*. Bellingham, Wash: SPIE Publications, 2001.
[46] J. Brown, “Artificial dielectrics having refractive indices less than unity,” *Proc. IEE - Part IV Inst. Monogr.*, vol. 100, no. 5, pp. 51–62, Oct. 1953, doi: 10.1049/pi-4.1953.0009.
[47] V. G. Veselago, “THE ELECTRODYNAMICS OF SUBSTANCES WITH SIMULTANEOUSLY NEGATIVE VALUES OF AND μ,” *Sov. Phys. Uspekhi*, vol. 10, no. 4, p. 509, Apr. 1968, doi: 10.1070/PU1968v010n04ABEH003699.
[48] J. B. Pendry, “Negative Refraction Makes a Perfect Lens,” *Phys. Rev. Lett.*, vol. 85, no. 18, pp. 3966–3969, Oct. 2000, doi: 10.1103/PhysRevLett.85.3966.
[49] W. J. Padilla, D. N. Basov, and D. R. Smith, “Negative refractive index metamaterials,” *Mater. Today*, vol. 9, no. 7, pp. 28–35, Jul. 2006, doi: 10.1016/S1369-7021(06)71573-5.
[50] N. Engheta, *Metamaterials : Physics and Engineering Explorations*. 2006. doi: 10.1002/0471784192.

[51] P. Moitra, Y. Yang, Z. Anderson, I. I. Kravchenko, D. P. Briggs, and J. Valentine, "Realization of an all-dielectric zero-index optical metamaterial," *Nat. Photonics*, vol. 7, no. 10, Art. no. 10, Oct. 2013, doi: 10.1038/nphoton.2013.214.
[52] J. Jiao, *The Simulation And Structure Design of Optical Metamaterials*. The University of Manchester (United Kingdom), 2013.
[53] K. Diest, Ed., *Numerical Methods for Metamaterial Design*, 2013th edition. New York: Springer, 2013.
[54] W. Cai, V. Shalaev, and D. Paul, "Optical Metamaterials: Fundamentals and Applications," *Phys. Today - PHYS TODAY*, vol. 63, Sep. 2010, doi: 10.1063/1.3490504.
[55] N. M. Litchinitser and V. M. Shalaev, "Optical Metamaterials: Invisibility in Visible and Nonlinearities in Reverse," in *Nonlinearities in Periodic Structures and Metamaterials*, C. Denz, S. Flach, and Y. S. Kivshar, Eds., in Springer Series in Optical Sciences. Berlin, Heidelberg: Springer, 2010, pp. 217–240. doi: 10.1007/978-3-642-02066-7_13.
[56] W. M. Telford, L. P. Geldart, and R. E. Sheriff, *Applied Geophysics*. Cambridge University Press, 1990.
[57] X. C. Tong, *Functional Metamaterials and Metadevices*, 1st ed. 2018 edition. New York, NY: Springer, 2017.
[58] A. Zagoskin, D. Felbacq, and E. Rousseau, "Quantum metamaterials in the microwave and optical ranges," *EPJ Quantum Technol.*, vol. 3, Feb. 2016, doi: 10.1140/epjqt/s40507-016-0040-x.
[59] A. M. Zagoskin, D. Felbacq, and E. Rousseau, "Quantum metamaterials in the microwave and optical ranges," *EPJ Quantum Technol.*, vol. 3, no. 1, p. 2, Feb. 2016, doi: 10.1140/epjqt/s40507-016-0040-x.
[60] S. Choudhury *et al.*, "Material platforms for optical metasurfaces," *Nanophotonics*, vol. 7, May 2018, doi: 10.1515/nanoph-2017-0130.
[61] N. I. Zheludev, "A Roadmap for Metamaterials," *Opt. Photonics News*, vol. 22, no. 3, pp. 30–35, Mar. 2011, doi: 10.1364/OPN.22.3.000030.
[62] X. Luo, M. Pu, X. Ma, and X. Li, "Taming the Electromagnetic Boundaries via Metasurfaces: From Theory and Fabrication to Functional Devices," *Int. J. Antennas Propag.*, vol. 2015, p. e204127, Oct. 2015, doi: 10.1155/2015/204127.
[63] B. Luk'yanchuk *et al.*, "The Fano resonance in plasmonic nanostructures and metamaterials," *Nat. Mater.*, vol. 9, no. 9, pp. 707–715, Sep. 2010, doi: 10.1038/nmat2810.
[64] "Plasmon." https://www.researchgate.net/publication/260688545_Combined_Optical_and_Electrical_Design_of_Plasmonic_Back_Reflector_for_High-Efficiency_Thin-Film_Silicon_Solar_Cells (accessed May 19, 2023).
[65] C. Simovski and S. Tretyakov, *An Introduction to Metamaterials and Nanophotonics*. Cambridge: Cambridge University Press, 2020. doi: 10.1017/9781108610735.
[66] P. B. Johnson and R. W. Christy, "Optical Constants of the Noble Metals," *Phys. Rev. B*, vol. 6, no. 12, pp. 4370–4379, Dec. 1972, doi: 10.1103/PhysRevB.6.4370.
[67] M. A. Ordal, R. J. Bell, R. W. Alexander, L. L. Long, and M. R. Querry, "Optical properties of fourteen metals in the infrared and far infrared: Al, Co, Cu, Au, Fe, Pb, Mo, Ni, Pd, Pt, Ag, Ti, V, and W.," *Appl. Opt.*, vol. 24, no. 24, pp. 4493–4499, Dec. 1985, doi: 10.1364/AO.24.004493.
[68] S. A. Maier, *Plasmonics: Fundamentals and Applications*. New York, NY: Springer US, 2007. doi: 10.1007/0-387-37825-1.

[69] S. Morawiec and I. Crupi, “Light trapping by plasmonic nanoparticles,” in *Solar Cells and Light Management*, Elsevier, 2020, pp. 277–313.
[70] A. J. Morfa, K. L. Rowlen, T. H. Reilly, M. J. Romero, and J. van de Lagemaat, “Plasmon-enhanced solar energy conversion in organic bulk heterojunction photovoltaics,” *Appl. Phys. Lett.*, vol. 92, p. 013504, Jan. 2008, doi: 10.1063/1.2823578.
[71] C. F. Bohren and D. R. Huffman, *Absorption and Scattering of Light by Small Particles*. John Wiley & Sons, 2008.
[72] N. C. Lindquist, P. Nagpal, K. M. McPeak, D. J. Norris, and S.-H. Oh, “Engineering metallic nanostructures for plasmonics and nanophotonics,” *Rep. Prog. Phys.*, vol. 75, no. 3, p. 036501, Feb. 2012, doi: 10.1088/0034-4885/75/3/036501.
[73] S. Morawiec, M. J. Mendes, S. Mirabella, F. Simone, F. Priolo, and I. Crupi, “Self-assembled silver nanoparticles for plasmon-enhanced solar cell back reflectors: correlation between structural and optical properties,” *Nanotechnology*, vol. 24, no. 26, p. 265601, Jul. 2013, doi: 10.1088/0957-4484/24/26/265601.
[74] K. R. Catchpole and A. Polman, “Design principles for particle plasmon enhanced solar cells,” *Appl. Phys. Lett.*, vol. 93, no. 19, p. 191113, Nov. 2008, doi: 10.1063/1.3021072.
[75] S. Pillai, F. J. Beck, K. R. Catchpole, Z. Ouyang, and M. A. Green, “The effect of dielectric spacer thickness on surface plasmon enhanced solar cells for front and rear side depositions,” *J. Appl. Phys.*, vol. 109, no. 7, p. 073105, Apr. 2011, doi: 10.1063/1.3567299.
[76] F. J. Beck, S. Mokkapati, and K. R. Catchpole, “Light trapping with plasmonic particles: beyond the dipole model,” *Opt. Express*, vol. 19, no. 25, pp. 25230–25241, Dec. 2011, doi: 10.1364/OE.19.025230.
[77] Z. Ouyang, X. Zhao, S. Varlamov, Y. Tao, J. Wong, and S. Pillai, “Nanoparticle-enhanced light trapping in thin-film silicon solar cells,” *Prog. Photovolt. Res. Appl.*, vol. 19, pp. 917–926, Dec. 2011, doi: 10.1002/pip.1135.
[78] V. E. Ferry, M. A. Verschuuren, M. C. van Lare, R. E. I. Schropp, H. A. Atwater, and A. Polman, “Optimized Spatial Correlations for Broadband Light Trapping Nanopatterns in High Efficiency Ultrathin Film a-Si:H Solar Cells,” *Nano Lett.*, vol. 11, no. 10, pp. 4239–4245, Oct. 2011, doi: 10.1021/nl202226r.
[79] U. W. Paetzold *et al.*, “Plasmonic reflection grating back contacts for microcrystalline silicon solar cells,” *Appl. Phys. Lett.*, vol. 99, no. 18, p. 181105, Oct. 2011, doi: 10.1063/1.3657513.
[80] H. Tan, R. Santbergen, A. H. M. Smets, and M. Zeman, “Plasmonic Light Trapping in Thin-film Silicon Solar Cells with Improved Self-Assembled Silver Nanoparticles,” *Nano Lett.*, vol. 12, no. 8, pp. 4070–4076, Aug. 2012, doi: 10.1021/nl301521z.
[81] H. Tan, R. Santbergen, G. Yang, A. H. Smets, and M. Zeman, “Combined optical and electrical design of plasmonic back reflector for high-efficiency thin-film silicon solar cells,” in *2012 IEEE 38th Photovoltaic Specialists Conference (PVSC) PART 2*, IEEE, 2012, pp. 1–6.
[82] H. Tan, L. Sivec, B. Yan, R. Santbergen, M. Zeman, and A. H. M. Smets, “Improved light trapping in microcrystalline silicon solar cells by plasmonic back reflector with broad angular scattering and low parasitic absorption,” *Appl. Phys. Lett.*, vol. 102, no. 15, p. 153902, Apr. 2013, doi: 10.1063/1.4802451.
[83] A. Bossavit and I. Mayergoyz, *Computational electromagnetism variational formulations, complementarity, edge elements / Alain Bossavit.*, 1st edition. in Electromagnetism. San Diego: Academic Press, 1998.

[84] T. Rylander, P. Ingelström, and A. Bondeson, *Computational Electromagnetics*. in Texts in Applied Mathematics. New York, NY: Springer, 2013. doi: 10.1007/978-1-4614-5351-2.
[85] J. Bergin and J. R. Guerci, *MIMO Radar: Theory and Application*. Boston: Artech House, 2018.
[86] J. Li and Y. Huang, "Time-Domain Finite Element Methods for Metamaterials," 2013, pp. 53–125. doi: 10.1007/978-3-642-33789-5_3.
[87] J. Li and Y. Huang, *Time-Domain Finite Element Methods for Maxwell's Equations in Metamaterials*, 2013th edition. Heidelberg: Springer, 2012.
[88] R. Courant, "Variational methods for the solution of problems of equilibrium and vibrations," *Bull. Am. Math. Soc.*, vol. 49, no. 1, pp. 1–23, Jan. 1943.
[89] S. Ahmed and P. Daly, "Waveguide solutions by the finite-element method," *Radio Electron. Eng.*, vol. 38, no. 4, pp. 217–223, Oct. 1969, doi: 10.1049/ree.1969.0103.
[90] "CST Studio Suite Help." https://space.mit.edu/RADIO/CST_online/cst_studio_suite_help.htm (accessed May 21, 2023).
[91] Q. Ni, H. Alshehri, Y. Yang, H. Ye, and L. Wang, "Plasmonic light trapping for enhanced light absorption in film-coupled ultrathin metamaterial thermophotovoltaic cells," *Front. Energy*, vol. 12, no. 1, pp. 185–194, Mar. 2018, doi: 10.1007/s11708-018-0522-x.
[92] L. P. Wang and Z. M. Zhang, "Wavelength-selective and diffuse emitter enhanced by magnetic polaritons for thermophotovoltaics," *Appl. Phys. Lett.*, vol. 100, no. 6, p. 063902, Feb. 2012, doi: 10.1063/1.3684874.
[93] P. West, S. Ishii, G. Naik, N. Emani, V. M. Shalaev, and A. Boltasseva, "Searching for Better Plasmonic Materials." arXiv, Mar. 30, 2010. Accessed: Mar. 27, 2023. [Online]. Available: http://arxiv.org/abs/0911.2737
[94] R. Ferrini, M. Patrini, and S. Franchi, "Optical functions from 0.02 to 6 eV of AlxGa1−xSb/GaSb epitaxial layers," *J. Appl. Phys.*, vol. 84, no. 8, pp. 4517–4524, Oct. 1998, doi: 10.1063/1.368677.
[95] B. J. Lee, L. P. Wang, and Z. M. Zhang, "Coherent thermal emission by excitation of magnetic polaritons between periodic strips and a metallic film," *Opt. Express*, vol. 16, no. 15, pp. 11328–11336, Jul. 2008, doi: 10.1364/oe.16.011328.
[96] L. P. Wang and Z. M. Zhang, "Wavelength-selective and diffuse emitter enhanced by magnetic polaritons for thermophotovoltaics," *Appl. Phys. Lett.*, vol. 100, no. 6, Feb. 2012, doi: 10.1063/1.3684874.
[97] B. Zhao, L. Wang, Y. Shuai, and Z. M. Zhang, "Thermophotovoltaic emitters based on a two-dimensional grating/thin-film nanostructure," *Int. J. Heat Mass Transf.*, vol. 67, pp. 637–645, Dec. 2013, doi: 10.1016/j.ijheatmasstransfer.2013.08.047.
[98] H. Wang and L. Wang, "Tailoring thermal radiative properties with film-coupled concave grating metamaterials," *J. Quant. Spectrosc. Radiat. Transf.*, vol. 158, pp. 127–135, Jun. 2015, doi: 10.1016/j.jqsrt.2014.11.015.
[99] J. Zhou, E. N. Economon, T. Koschny, and C. M. Soukoulis, "Unifying approach to left-handed material design," *Opt. Lett.*, vol. 31, no. 24, pp. 3620–3622, Dec. 2006, doi: 10.1364/ol.31.003620.
[100] H. Wang and L. Wang, "Tailoring thermal radiative properties with film-coupled concave grating metamaterials," *J. Quant. Spectrosc. Radiat. Transf.*, vol. 158, pp. 127–135, 2015.
[101] Z. Zhang, *Nano/Microscale Heat Transfer*, 1st edition. New York, NY: McGraw-Hill Education, 2007.

[102] L. P. Wang, B. J. Lee, X. J. Wang, and Z. M. Zhang, “Spatial and temporal coherence of thermal radiation in asymmetric Fabry–Perot resonance cavities,” *Int. J. Heat Mass Transf.*, vol. 52, no. 13, pp. 3024–3031, Jun. 2009, doi: 10.1016/j.ijheatmasstransfer.2009.01.042.
[103] “Tailoring thermal radiative properties with film-coupled concave grating metamaterials - ScienceDirect.” https://www.sciencedirect.com/science/article/abs/pii/S002240731400466X (accessed Mar. 13, 2023).
[104] L. Zhang, L. Tang, W. Wei, X. Cheng, W. Wang, and H. Zhang, “Enhanced near-infrared absorption in graphene with multilayer metal-dielectric-metal nanostructure,” *Opt. Express*, vol. 24, no. 18, pp. 20002–20009, Sep. 2016, doi: 10.1364/OE.24.020002.
[105] K. Park, S. Basu, W. P. King, and Z. M. Zhang, “Performance analysis of near-field thermophotovoltaic devices considering absorption distribution,” *J. Quant. Spectrosc. Radiat. Transf.*, vol. 109, no. 2, pp. 305–316, Jan. 2008, doi: 10.1016/j.jqsrt.2007.08.022.
[106] L. Tang, C. Xu, and X. Chen, “Comparison of the Performance of GaInAsSb and GaSb Cells under Different Temperature Blackbody Radiations,” Aug. 2016, doi: 10.5281/zenodo.1126712.
[107] T. L. Bergman, T. L. Bergman, F. P. Incropera, D. P. DeWitt, and A. S. Lavine, *Fundamentals of Heat and Mass Transfer*. John Wiley & Sons, 2011.
[108] Q. Ni, H. Ye, Y. Shu, and Q. Lin, “A theoretical discussion on the internal quantum efficiencies of the epitaxial single crystal GaSb thin film cells with different p–n junctions,” *Sol. Energy Mater. Sol. Cells*, vol. 149, pp. 88–96, May 2016, doi: 10.1016/j.solmat.2015.12.039.